

Clinopyroxene/melt trace-element-partitioning in sodic alkaline magmas

Charles D. Beard^{a,b,*}, Vincent J. van Hinsberg^b, John Stix^b, Max Wilke^{c,d}

^a*British Geological Survey, The Lyell Centre, Research Avenue South, Edinburgh, EH14 4AP, UK*

^b*Earth and Planetary Sciences, McGill University, 3450 University Street, Montreal, Québec, H3A 0E8, Canada*

^c*Institut für Erd- und Umweltwissenschaften, Universität Potsdam, Golm, Germany*

^d*Chemie und Physik der Geomaterialien, Deutsches GeoForschungsZentrum GFZ, Potsdam, Germany*

Abstract

Clinopyroxene is a key fractionating phase in alkaline magmatic systems, but its impact on metal-enrichment processes, and the formation of REE + HFSE mineralisation in particular, are not well understood. To constrain the control of clinopyroxene on REE + HFSE behaviour in sodic (per)alkaline magmas, a series of internally heated pressure vessel experiments was performed to determine clinopyroxene-melt element-partitioning systematics. Synthetic tephriphonolite to phonolite compositions were run H_2O -saturated at 650–825°C with oxygen fugacity buffered to $\log f\text{O}_2 \approx \Delta\text{QFM} + 1$ or $\log f\text{O}_2 \approx \Delta\text{QFM} + 5$. Clinopyroxene-glass pairs from basanitic to phonolitic fall deposits from Tenerife, Canary Islands, were also measured to complement our experimentally derived data set.

The REE partition coefficients are 0.3–53, typically 2–6, with minima for

*corresponding author

Email address: cbeard@bgs.ac.uk (Charles D. Beard)

high-aegirine clinopyroxene. Diopside-rich clinopyroxene (Ae_{5-25}) prefer the MREE and have high REE partition coefficients (D_{Eu} up to 53, D_{Sm} up to 47). As clinopyroxene become more Na- and less Ca-rich (Ae_{25-50}), REE incorporation becomes less favourable, and both the M1 and M2 sites expand (to 0.79 Å and 1.12 Å), increasing D_{LREE}/D_{MREE} . Above Ae_{50} , both M sites shrink slightly and HREE ($V^I r_i \leq 0.9 \text{ \AA} \approx \text{Y}$) partition strongly onto the M1 site, consistent with a reduced charge penalty for $\text{REE} \leftrightarrow \text{Fe}^{3+}$ substitution.

Our data, complemented with an extensive literature database, constrain a model that predicts trace-element-partition coefficients between clinopyroxene and silicate melt using only mineral major-element compositions, temperature and pressure as input. The model is calibrated for use over a wide compositional range and can be used to interrogate clinopyroxene from a variety of natural systems to determine the trace-element concentrations in their source melts, or to forward model the trace-element evolution of tholeiitic mafic to evolved peralkaline magmatic systems.

Keywords: rare earth elements, aegirine, experimental petrology, Canary Islands, phonolite, peralkaline

1. Introduction

Sodic clinopyroxene appear to more readily incorporate REE than their calcic equivalents (Marks et al., 2004), but despite fractionation of these minerals, melts in evolved alkaline systems can attain high REE contents, even up to economic levels (Kogarko, 1990; Downes et al., 2005; Marks et al., 2011; Sjöqvist et al., 2013; Goodenough et al., 2016; Möller and Williams-Jones, 2016). Trace-element data may be used to model magmatic processes (Spera and Bohrson, 2001; Troll and Schmincke, 2002; Boudreau, 2004; Xu et al., 2010; Girnis et al., 2013; Mungall and Brenan, 2014), but their interpretation requires precise knowledge of mineral/liquid element-partition coefficients. The approach has been applied to studies of mafic systems and mantle melting processes (Niu, 2004; Workman and Hart, 2005; Foley et al., 2013; Coumans et al., 2016; Peters et al., 2017). However, poor constraints on element-partitioning behaviour in alkaline and peralkaline rocks thus far preclude widespread application in these systems.

Experimental investigations of element-partitioning behaviour in alkali-enriched systems are limited in terms of composition (Wood and Trigila, 2001; Huang et al., 2006), and none yet have explored peralkaline conditions where molar $(\text{Na}+\text{K})/\text{Al}$ exceeds 1. Additional information has been obtained from natural samples by measuring the concentration ratios of phenocryst–glass pairs from volcanic and intrusive rocks (Larsen, 1979; Wörner et al., 1983; Shearer and Larsen, 1994; Severs et al., 2009; Fedele et al., 2009; Mollo et al., 2016). However, these results may be biased by the presence of melt inclusions, mineral inclusions and mineral zoning, and their interpretation is commonly complicated by unknown or poorly constrained P-T-H₂O-*f*O₂ con-

²⁶ ditions of equilibration and assumptions of closed-system behaviour.

²⁷ In this contribution, we present trace-element-partition coefficients be-
²⁸ tween sodic clinopyroxene and silicate melts of tephriphonolite to phonolite
²⁹ composition, as determined from internally heated pressure vessel experi-
³⁰ ments on synthetic and natural compositions. These are complemented by
³¹ well-constrained natural volcanic phenocryst-glass pairs from Canary Islands
³² pyroclastic fall deposits. We characterise the mineral compositional controls
³³ on element-partitioning behaviour and present a predictive model for clinopy-
³⁴ roxene/melt element-partitioning that can be used to generate clinopyrox-
³⁵ ene/melt partition coefficients using only clinopyroxene major-element com-
³⁶ positions (e.g., as measured by electron-microprobe). This approach permits
³⁷ forward modelling of element budgets during differentiation processes in mag-
³⁸ matic systems, including evolved sodic alkaline systems, as well as providing
³⁹ a mineral-based tool that can be used to reconstruct parental melt composi-
⁴⁰ tions from clinopyroxene compositions in natural rocks.

⁴¹ 2. Methodology

⁴² 2.1. Experiment starting materials

⁴³ Clinopyroxene were synthesised in sodic alkaline silicate melts of varying
⁴⁴ composition to obtain a range of mineral compositions consistent with those
⁴⁵ in natural systems. Starting glass compositions are given in Table 1 and Fig-
⁴⁶ ure S1. Synthetic glasses L1 and L5 were prepared from reagent-grade oxide
⁴⁷ and carbonate powders, ground together in an agate mortar, decarbonated
⁴⁸ for 6 hrs at 450°C, then homogenised in air for 3 hrs at 1400°C in a Pt cru-
⁴⁹ cible. Repeated fusion and grinding in agate ensured chemical homogeneity

50 of the starting glasses, which was confirmed by electron-microprobe analyses
51 of the final fused glass. Finely-ground Mud Tank zircon was added to the
52 homogeneous major-element glasses as a source of Zr, Hf, Nb and Ta; the
53 glasses were then fused for a further three hours at 1400°C. The remaining
54 trace-elements were added as a cocktail of single-element nitrate solutions
55 (ICP-MS standards), dried onto the powdered glasses, then denitrified at
56 450°C for 30 minutes. The synthetic basanite L1 and phonolite L5 were
57 mixed in varying proportions to make the low alkali (L) series of starting
58 glasses, while dried NaOH and KOH powders were added to make the mid-
59 dle (M) and high (H) alkali starting glasses. Analyses of glass compositions
60 L5 and H5, quenched from superliquidus conditions, confirm that Henry's
61 law was respected (Supplement S1).

62 A well-mixed rock powder from the Nechalacho Layered Suite in Canada
63 (Möller and Williams-Jones, 2016, Unit NLS-9, sample L09-194-405.5, al-
64 ternative sample name VM 11-6) was used as experimental starting mate-
65 rial for a more extreme peralkaline composition. This composition was not
66 fused prior to loading into experiment capsules, so as to preserve the origi-
67 nal volatile-element concentrations. An experiment using this material that
68 was quenched from superliquidus conditions is homogeneous with respect to
69 major-elements, as determined from electron-microprobe measurements.

70 *2.2. Experimental equipment and procedures*

71 In total, 36 partitioning experiments were conducted in a Harwood-type
72 internally heated pressure vessel (IHPV) in the HP-GeoMatS laboratory at
73 the German GeoForschungsZentrum (Table S1). Temperature was measured
74 with Type-S thermocouples calibrated against the melting point of NaCl

⁷⁵ (Borchert et al., 2010, accuracy of ± 5 °C at 200 MPa). Argon gas was used
⁷⁶ as the pressure medium, and pressure was measured with a strain gauge to
⁷⁷ an accuracy of ± 7 MPa. During the experiments, pressure was controlled
⁷⁸ automatically and held within ± 5 MPa of stated values.

⁷⁹ Oxygen fugacity was buffered to the intrinsic redox conditions of the
⁸⁰ experimental setup, which corresponds to $\log f\text{O}_2 \text{ ca. } \Delta\text{QFM} + 1$ in our H_2O -
⁸¹ saturated charges (see Chou, 1986; Berndt et al., 2002; Jugo et al., 2010). One
⁸² experiment using the Nechalacho Layered Suite composition was performed
⁸³ in a double capsule with a haematite solid buffer, designed to increase $f\text{O}_2$
⁸⁴ and promote crystallisation of Fe^{3+} -rich clinopyroxene (Eugster and Wones,
⁸⁵ 1962). This experiment ran at the Hm-Mt buffer, which corresponds to
⁸⁶ $\log f\text{O}_2 \approx \Delta\text{QFM} + 5$, as confirmed by presence of both buffer minerals in
⁸⁷ the outer capsule following quench. The experiments were designed to run
⁸⁸ between the liquidus and solidus for each composition, which corresponds to
⁸⁹ temperatures between 650 and 825°C, all at 200 MPa pressure (Table S1).

⁹⁰ Powdered starting glass and distilled, deionised water were welded inside
⁹¹ 3.0 or 3.5 mm outer diameter platinum capsules of 20–25 mm length (see
⁹² Table S1). To verify that capsules were sealed, they were heated to 110°C
⁹³ and weighed before and after run. The amount of water sealed inside the
⁹⁴ capsules varied with temperature and composition and was kept in excess
⁹⁵ of saturation (Carroll and Blank, 1997; Moore et al., 1998; Schmidt and
⁹⁶ Behrens, 2008). Water saturation was confirmed post-run by puncturing
⁹⁷ capsules and checking for water expulsion and mass loss on drying at 110°C.

⁹⁸ The capsules were loaded into the vessel, pressurised to 200 MPa, then
⁹⁹ heated to superliquidus temperatures for at least 16 hrs (Table S1) to per-

mit homogenisation of trace-element concentrations, dissolution of water and equilibration of fO_2 by exchange of H_2 through the capsule wall (cf. Gaillard et al., 2002). Following homogenisation, temperature was lowered to run conditions. An initial set of experiments were cooled rapidly from homogenisation to run temperature at about 100°C/min. A second set of experiments were cooled to run temperature at 1°C/min to promote slow growth of crystals and to minimise the formation of compositional gradients in the melt. Vessel temperature was then cycled between run temperature and run temperature + 10°C to promote dissolution of small crystals at the expense of larger grains, and to promote crystal growth close to the run temperature. Element partitioning results are consistent among experiments of different cooling paths. In all experiments, run temperature was kept constant for at least 40 hrs to allow for chemical homogenisation of melt and growth of crystals via Ostwald ripening. Capsules were then quenched to room temperature.

To minimise the growth of groundmass crystals on cooling, a rapid-quench apparatus was used where possible (Table 2). We have not measured quench rates in this vessel, but the capsules probably cooled at rates of several hundred degrees Celcius per second (e.g. Berndt et al., 2002). For the rest of the experiments, quenching was achieved by cutting power to the furnace, which resulted in cooling to below the glass-transition temperature (< 350°C; Giordano et al., 2005) in less than 150 seconds.

2.3. Natural samples

Alkaline volcanism on Tenerife is associated with a weak thermal mantle plume that impinges upon thick, old, slow-moving oceanic lithosphere (Car-

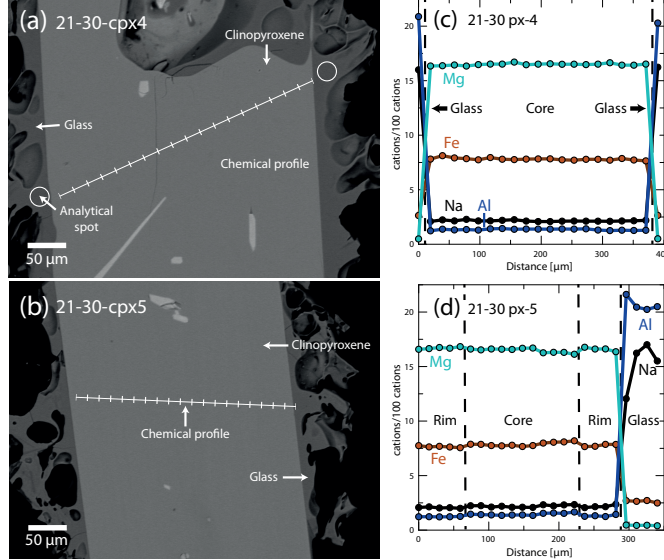


Figure 1: Examples of textural features from Canary Islands clinopyroxene phenocrysts from this study. (a, b) Backscattered electron images show that crystals are euhedral and are free from complex zoning patterns. (c, d) Chemical profiles across clinopyroxene phenocrysts and glass rims (quenched melt), as measured by wavelength dispersive spectroscopy, showing that zoning is effectively absent in these clinopyroxene. In (c) analyses of glass are aligned with the chemical profile shown in (a). Glass analyses shown in (d) are from rims of quenched melt from other clinopyroxene phenocrysts recovered from the same pumice sample. Both pictured phenocrysts are from the basal air fall deposit, associated with the ~ 2 ka eruption of Pico Viejo, Tenerife (Ablay et al., 1995).

racedo et al., 2007). This geological scenario has favoured development of a complex magma-plumbing system that produces a great diversity of volcanic products from alkali basalt to phonolite in composition. The Las Cañadas edifice, a large, central, composite stratovolcano (Bryan et al., 1998; Brown et al., 2003; Edgar et al., 2007), rests upon a base of at least three mafic al-

¹³⁰ kaline shield volcanoes (Thirlwall et al., 2000; Guillou et al., 2004; Gurenko
¹³¹ et al., 2006). Xenoliths indicate that a nepheline syenite intrusive system
¹³² underlies the island (Wiesmaier et al., 2012).

¹³³ Six clinopyroxene/glass pairs from four different volcanic eruptions on
¹³⁴ Tenerife have been investigated. The ~ 2 ka eruptive products of Montaña
¹³⁵ Blanca and Pico Viejo (Abhay et al., 1995) are phonolitic, plinian fall de-
¹³⁶ posits, whereas Montaña Samara is a monogenetic, mafic cinder cone (Albert
¹³⁷ et al., 2015). Phase-equilibrium experiments conducted on Montaña Blanca
¹³⁸ unit UMB-II suggest that magma was stored prior to eruption at $850 \pm 15^\circ\text{C}$,
¹³⁹ 50 ± 20 MPa, with 2.5 ± 0.5 wt% H₂O at $\log f\text{O}_2 \approx \text{NNO} - 0.5$ (Andújar and
¹⁴⁰ Scailet, 2012). Field locations, mineral proportions and major-element com-
¹⁴¹ positions of the clinopyroxene and glasses are presented in Table S1.

¹⁴² 2.4. Sample preparation

¹⁴³ Experiment capsules were torn open with pliers, and charges were split
¹⁴⁴ using a low-speed wafering saw. Samples were mounted in epoxy resin and
¹⁴⁵ polished for *in-situ* chemical analyses.

¹⁴⁶ Natural pyroclastic rocks were rinsed in tap water and crushed with a
¹⁴⁷ hammer. Crystals and glass fragments, hand-picked from a sieved size-
¹⁴⁸ fraction between 1.18 mm and 125 μm , were used to make grain mounts
¹⁴⁹ containing 5–20 crystals of clinopyroxene per sample. Natural samples also
¹⁵⁰ contain biotite, sanidine, \pm spinel, amphibole, olivine, titanite and sodalite.
¹⁵¹ Clinopyroxene mineral mounts were examined using backscattered electron
¹⁵² imaging to select euhedral crystals that were free from melt inclusions and
¹⁵³ chemical zoning ($n = 6$, Fig. 1).

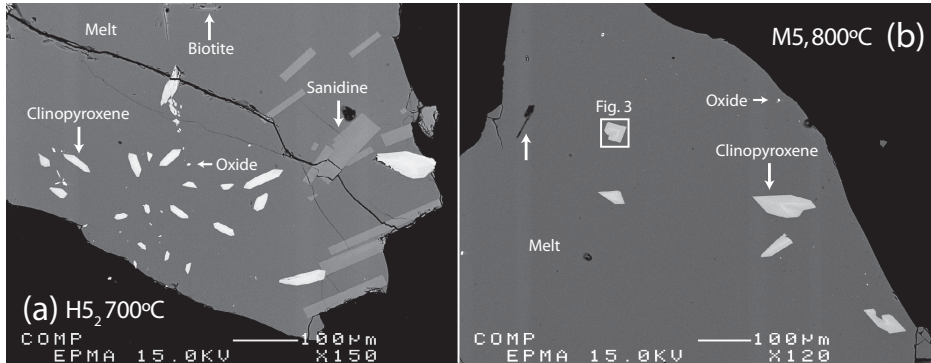


Figure 2: Backscattered electron images showing typical textures of run products from the internally heated pressure vessel experiments. Crystal fractions are typically small (<10% by area), with blade-shaped, euhedral clinopyroxene and glasses free of quench crystals.

¹⁵⁴ **3. Analytical techniques**

¹⁵⁵ All experimental products were examined by reflected-light optical mi-
¹⁵⁶ croscopy and scanning electron microscopy, and all phases produced were
¹⁵⁷ identified by electron-microprobe using an energy-dispersive detector. Im-
¹⁵⁸ ages were obtained to estimate modal proportions of phases, which were
¹⁵⁹ calculated using ImageJ freeware (Rasband, 2016, see Table S1).

¹⁶⁰ *3.1. Electron-microprobe analysis*

¹⁶¹ Major-element compositions of experimental products and natural min-
¹⁶² erals and glasses were measured with a JEOL 8900 instrument at McGill
¹⁶³ University and a JEOL 8230 instrument at the University of Ottawa (Table
¹⁶⁴ 3). An accelerating voltage of 15 kV was used with a 15 nA beam of 5 μm
¹⁶⁵ diameter for minerals, and a 4 nA beam of 50 μm diameter for glasses. Count
¹⁶⁶ times for all elements were 60 sec. Using the above routine, we observed no
¹⁶⁷ sodium loss over the measurement time period. For the silicate minerals and

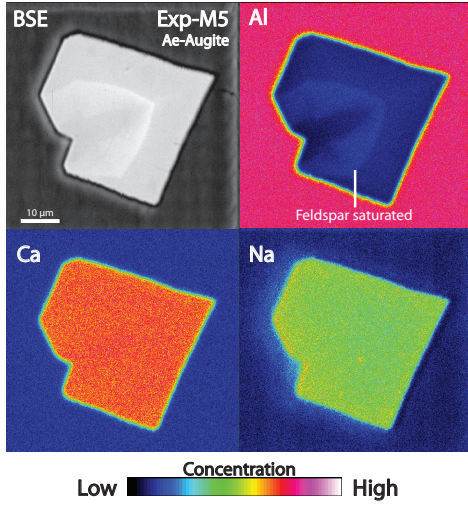


Figure 3: Element maps of clinopyroxene from internally heated pressure vessel experiment M5 (see box in lower magnification image, Fig. 2b). Aegirine-augite clinopyroxene have a sharp internal boundary that reflects feldspar saturation and are subtly zoned. Further element maps are available as an electronic supplement (Fig. S3).

¹⁶⁸ glasses, both synthetic and natural minerals or oxides were used for calibra-
¹⁶⁹ tion (see Table S1). Analytical uncertainties were determined by multiple
¹⁷⁰ analyses of reference materials and duplicate analyses of samples.

¹⁷¹ Element distribution maps were generated with a JEOL 8900 instrument
¹⁷² at McGill University using an accelerating voltage of 15 kV, a focussed 40
¹⁷³ nA beam, and a dwell time of 50 ms per pixel (Figs. 3, S3). Fe, Ti, Al, Si
¹⁷⁴ and Na were measured with wavelength-dispersive detectors, while Ca and
¹⁷⁵ Mg were measured with an energy-dispersive spectrometer.

¹⁷⁶ Transects of Ce, Mg and Fe concentrations within the experiment clinopy-
¹⁷⁷ roxene were measured with a JEOL 8900 instrument at McGill University
¹⁷⁸ using a focussed beam of 50 nA with an accelerating voltage of 20 kV. Ce was

179 counted with a wavelength-dispersive spectrometer with an LIFH crystal for
180 100 sec (MAC-Ce standard). Mg and Fe were counted for 20 sec, with TAP
181 and LIF crystals respectively (diopside and olivine standards, respectively).
182 Matrix corrections for Mg, Fe and Ce were not possible with these data, for
183 lack of other major-elements measured, however their relative values may
184 still be used to assess the extent to which the clinopyroxene are chemically
185 zoned.

186 *3.2. Laser-ablation ICP-MS*

187 Trace-element concentrations of clinopyroxene and glasses were deter-
188 mined by laser-ablation ICP mass-spectrometry. Analyses were performed
189 at McGill University using a NewWave 213 nm Nd-YAG laser system coupled
190 to a Thermo Finnigan iCAP-Qc quadrupole ICP-MS instrument. Typical flu-
191 ence was 3–12 J/cm² (from 80 μm to 8 μm spot sizes), with a repetition rate
192 of 10 Hz. Ablated material was transferred to the ICP-MS in a He flow of 800
193 mL/min and mixed with Ar prior to injection into the plasma. Instrumental
194 drift was monitored by repeat analyses of the primary standard glass BCR-
195 2G, with bias monitored by repeat analyses of secondary standards UTR-2
196 peralkaline rhyolite and USGS-RGM-1 rhyolite glasses (Table S1). Sample
197 surfaces were pre-ablated to remove residues from polishing materials and to
198 improve ablation efficiency.

199 Primary and secondary standards and an unzoned Canary Islands clinopy-
200 roxene were analysed with beam sizes of 8–80 μm to monitor crater-size-
201 dependent element-fractionation effects; none were found for the elements
202 reported here. For minerals and glasses in the experimental charges, beam
203 sizes of 8–40 μm and 16–80 μm were used, respectively. Depending on grain-

204 size and availability, 5–14 mineral grains and 3–10 areas of glass were anal-
205 ysed per charge. Natural clinopyroxene and rim glasses were analysed using
206 a beam size of 12–80 μm and 12–30 μm , respectively. Wherever possible,
207 ablation was performed along lines parallel to crystal rims (1–3 $\mu\text{m} / \text{sec}$).

208 Drift corrections and data reduction were conducted in Iolite v2.5 (Paton
209 et al., 2011). The total of major-elements measured by LA-ICP-MS or, where
210 available, the Al concentration from electron-microprobe analyses, was used
211 as an internal standard (Table 3). For some experiments, ablation through
212 the minerals was too rapid to generate a stable signal for data-reduction
213 purposes. In these cases, a mixing model was applied to estimate the com-
214 position of these clinopyroxene, similar to those applied by Rubatto and
215 Hermann (2007); Yang et al. (2018, see supplementary methods S5)).

216 4. Results

217 4.1. Run product phase stability and crystallinity

218 Trace-element partition-coefficients are reported for eleven experimental
219 charges. 25 additional experiments were rejected as their run temperatures
220 were superliquidus or subsolidus, or because their growth textures were in-
221 dicative of disequilibrium (e.g. Fig. S3). Phase proportions are provided in
222 Table S1.

223 All reported experimental runs were near-liquidus (3–22% crystals, RL
224 images) and are characterised by a homogeneous distribution of phases (Fig
225 2), except for experiments H5₃ and NLS-9_{2-HM}, in which sanidine crystals
226 are concentrated at the centre. Glasses are clean, homogeneous and show a
227 limited range of major- and trace-element compositions for each experiment

(Fig. S1). Clinopyroxene crystals are generally small, euhedral blades with a narrow range of sizes for a given experiment (<10 μm to 100 μm in cross section, Figs. 2–3). In addition to clinopyroxene and glass, experiments on mafic to intermediate compositions produced magnetite, titanite \pm kaersutite amphibole, whereas some phonolitic experiments produced biotite, alkali feldspar \pm magnetite (Table S1).

Constraining the full phase equilibria of all of the investigated compositions was beyond the scope of this study. However, in our experiments it can be seen that clinopyroxene has a wide stability field across the investigated physicochemical conditions with only a single starting composition generating amphibole in place of pyroxene (experiments L3 and L3₂). Run conditions and run products given in Supplement S1.

4.2. Glass compositions

All run-product glasses are homogeneous across the length and breadth of the experiment capsules based on multiple electron-microprobe and laser-ablation ICP-MS analyses. Most major-element oxide compositions, as measured by electron-microprobe, show relative standard deviations of < 5% within experiment capsules, with minor-elements oxides (concentration < 1%) showing greater variability, most with standard deviations between 5 and 10 % relative. Trace-element-compositions of the glass, as measured by laser-ablation ICP-MS, typically show time-weighted relative standard deviations of 1 to 8% within each capsule, with this variability depending on both the absolute concentration of that element and on the beam-size that was used for analyses (Supplement S1). Low sum-totals of major-element oxide concentrations in the electron-microprobe analyses are a result of high

253 dissolved-water contents in the quenched melt.

254 On a total-alkalies vs. silica diagram the experiment glasses are predom-
255 inantly phonolitic in composition, though span the trachyte-phonolite join
256 (Fig. S1). Their alkalinity index (molar $(\text{Na} + \text{K})/\text{Al}$) is 0.85 to 1.40, cross-
257 ing the alkaline–peralkaline join, and the Mg# of these quenched melts is 0
258 (Mg-free) to 22. The dissolved water content of these quenched melts is 8.8
259 to 10.7 wt.% (by difference method from EPMA data, with the Fe oxidation
260 state assigned following Kress and Carmichael 1991) and their NBO/T ratios
261 are 0.98 to 1.42 (Mysen et al., 1982, 1985). The halogen content of the syn-
262 thetic experiments is nominally zero, whereas glasses from the Nechalacho
263 Layered Suite composition experiments typically contain 0.1 % F and 0.02
264 % Cl by weight.

265 The Canary Islands glasses are mostly trachytic to phonolitic, with one
266 basaltic trachy-andesite (sample 17-12, Montaña Samara), and are alkaline
267 to weakly peralkaline in composition (A.I. of 0.78 to 1.16) with Mg# of
268 8 to 39. Dissolved water content and NBO/T ratios are not reported for
269 these glasses because of post-eruptive loss of volatiles. These Canary Islands
270 glasses typically contain 0.2 % F and 0.4 % Cl by weight.

271 *4.3. Compositions of the clinopyroxene and major-element exchange*

272 Experiments on the synthetic compositions produced clinopyroxene of
273 diopside to aegirine-augite composition ($\text{Di}_{29-82}, \text{Ae}_{9-45} \text{ Hd}_{7-33}$), a subset of
274 which overlap with the compositional space defined by the Canary Islands
275 clinopyroxene on a diopside–hedenbergite–aegirine ternary diagram (Fig. 4,
276 Tables 3 and S1). This low-aegirine group of synthetic clinopyroxene display
277 a positive correlation between ${}^{\text{IV}}\text{Al} + {}^{\text{IV}}\text{Fe}^{3+}$ (in the T-site) and ${}^{\text{VI}}\text{Ti}$ con-

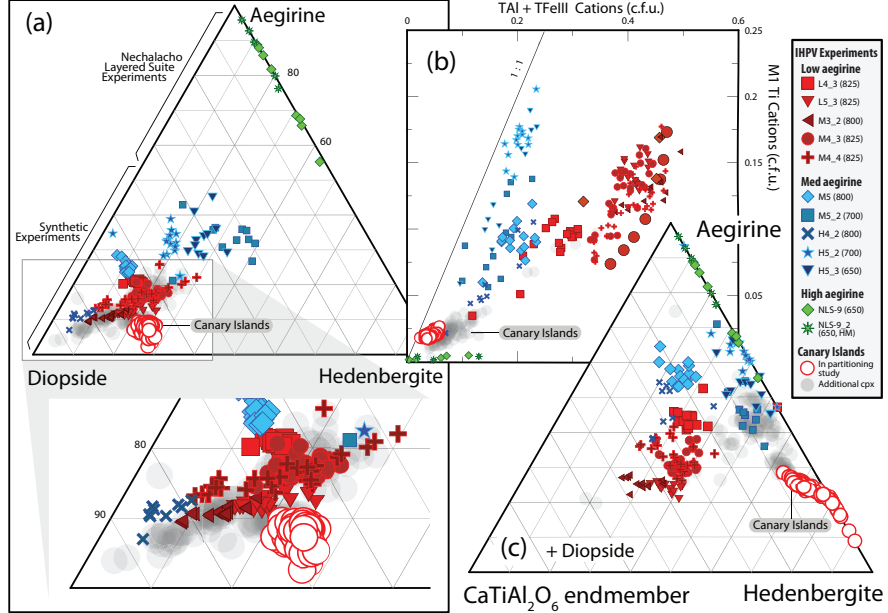


Figure 4: Clinopyroxene grown in internally heated pressure vessel experiments and separated from Canary Islands pyroclasts (a) expressed in terms of diopside, hedenbergite and aegirine end-members, (b) their M1Ti and tetrahedral Al and Fe³⁺ contents, and (c) expressed in terms of aegirine, hedenbergite and the theoretical CaTiAl₂O₆ end-member (Akasaka and Onuma, 1980). Fe²⁺/Fe³⁺ within the clinopyroxene was assigned following Droop (1987), then site occupancies and end-member proportions were allocated following Morimoto (1989). For methods used in calculation of the end-member proportions see Supplement S5. The range of clinopyroxene compositions within each experiment records changes to the composition of the melt during crystal growth, whereby the cores of the crystals record the first stage of crystallisation and the rims (highest Fe, Na) are in equilibrium with the quenched melt. Rims of these clinopyroxene are preferentially sampled in trace-element analyses by LA-ICP-MS.

278 tent (in the M1 site, red, *low aegirine*, Ae_{5–25}), and notably contain both
 279 of these elements at elevated concentration relative to the Canary Islands

280 clinopyroxene ($^{IV}\text{Al} + ^{IV}\text{Fe}^{3+} = 0.20\text{--}0.49$ c.f.u., $^{VI}\text{Ti} = 0.07\text{--}0.17$ c.f.u.). A
281 further subset of synthetic clinopyroxene have higher aegirine content (blue,
282 *med aegirine*, Ae_{25–50}) and show a similar range of Ti content to the low
283 aegirine synthetic minerals (0.05–0.18 c.f.u.), but a limited range of lower
284 $^{IV}\text{Al} + ^{IV}\text{Fe}^{3+}$ content (0.1–0.25 c.f.u., Fig. 4b). Experiments performed on
285 the Nechalacho Layered Suite composition (NLS-9, NLS-9_{2–HM}, green, *high*
286 *aegirine*, Ae_{55–95}) reproduced the aegirine-augite to aegirine clinopyroxene
287 from the natural system (Möller and Williams-Jones, 2016) that contain low
288 concentrations of $^{IV}\text{Al} + ^{IV}\text{Fe}^{3+}$ (up to 0.14 c.f.u.) and almost no Ti or Mg.

289 The Canary Islands clinopyroxene that were selected for determination
290 of mineral–melt partition coefficients are diopside in composition (Di_{65–71},
291 Ae_{3–10} Hd_{21–28}), with most crystals containing about 0.05 c.f.u. $^{IV}\text{Al} +$
292 $^{IV}\text{Fe}^{3+}$ and 0.02 c.f.u. ^{VI}Ti (Fig. 4). These minerals are free from melt in-
293 clusions, suggesting relatively slow rates of crystal growth (Kennedy et al.,
294 1993, Fig. 1). Chemical zonation, if present, is of a similar magnitude to
295 the analytical precision of our electron microprobe, indicating that pressure,
296 temperature and melt composition remained stable during crystal growth.
297 Trace-element abundances within these Canary Islands clinopyroxene show
298 core-to-rim variations of about 1–5 % relative, with larger variations in ele-
299 ment abundance associated with sector zoning than with concentric growth
300 zoning (Supplement S1).

301 By contrast our experiment clinopyroxene display systematic composi-
302 tional variation between their cores and rims; this variation recording changes
303 to melt composition during growth of these crystals (e.g. Fig. 3). The sys-
304 tematics of crystal-chemical zonation both within individual experimental

305 charges and within groups of experiments reveal major-element exchange
306 vectors between the clinopyroxene and the melt. Three major-element ex-
307 change mechanisms correspond to the low (Ae_{5-25}), medium (Ae_{25-50}) and
308 high (Ae_{55-95}) aegirine domains defined above (Figs. 4b, 5 and S4).

309 **And may be used to infer.... the composition of the mineral**
310 **assemblage that is crystallising? To discuss. Comments, please!**

311 With increasing alkali content, the Si content in clinopyroxene increases
312 at the expense of tetrahedrally co-ordinated Al and Fe^{3+} . As aegirine content
313 increases, substitutions at the tetrahedral site become relatively less impor-
314 tant than exchanges at the M1 and M2 sites. At the M1 site, the substitution
315 of Ti for ions of 2+ and 3+ valence correlates well with the exchange of tetra-
316 hedrally coordinated 3+ cations for Si^{4+} . The exchange behaviour of 2+ and
317 3+ cations at the M1 site depends on the aegirine content of the clinopy-
318 roxene. In low-aegirine clinopyroxene, the concentration of 3+ ions at the
319 M1 site is negatively correlated with X_{Na}^{M2} , whereas in medium- and high-
320 aegirine clinopyroxene, the M1 site takes progressively more 3+ ions as X_{Na}^{M2}
321 increases. Substitutions of Ca^{M2} for Na^{M2} are relatively unimportant in low-
322 aegirine clinopyroxene, but play a large role in medium- and high-aegirine
323 exchange vectors.

324 *4.4. Trace-element concentrations in the experiment clinopyroxene*

325 Assessing the homogeneity of trace-element-concentrations within min-
326 erals is important when defining mineral–melt partition-coefficients because
327 only the crystal rims record true chemical equilibrium with the adjacent melt.
328 In the case of experimental studies, trace-element analyses of crystal rims are
329 rarely possible because the mineral grains are commonly comparable in scale

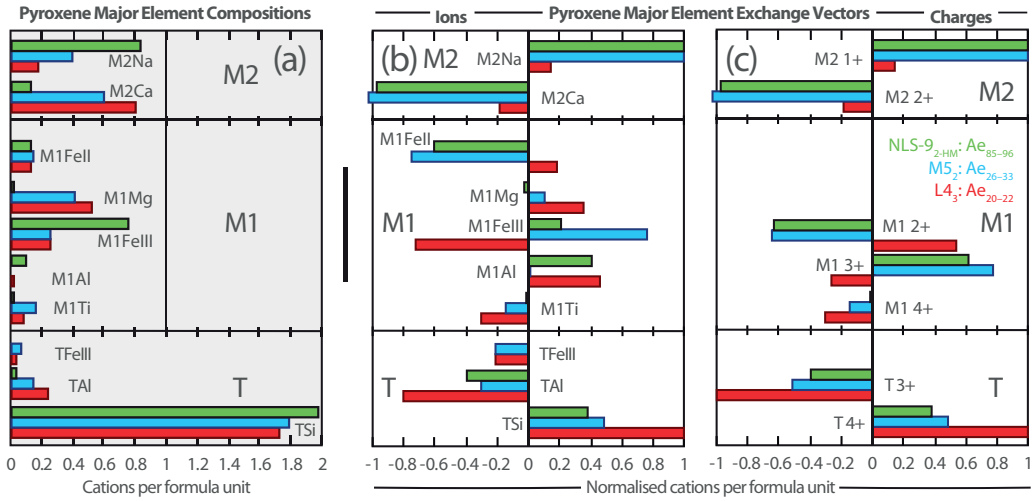


Figure 5: Bar charts showing clinopyroxene composition and major-element exchange mechanisms for three experiments representative of high (green), medium (blue) and low-aegirine (red) clinopyroxene. (a) clinopyroxene major-element compositions are expressed as cations per six-oxygen formula unit (b) exchange mechanisms grouped by ions, (c) grouped by charges. Methods used to calculate these exchange mechanisms are available in the caption of Supplementary Figure S4.

to the beam-size of laser-ablation or SIMS systems ($\sim 10 - 20 \mu\text{m}$).

To quantify the extent to which trace-element-concentrations are zoned within our experiment clinopyroxene, we measured electron-microprobe transects for the elements Mg, Fe and Ce across seven crystals from three experiments, each crystallised to varying degrees (Supplement S3). These transects reveal that clinopyroxene Ce-concentration follows both sector-zoning and concentric growth-zoning patterns, as recorded by backscattered electron images and the $X\text{Mg}$ of the clinopyroxene. Sector-zoning has a more pronounced effect on the Ce-concentration in the clinopyroxene than concentric

339 growth-zoning, causing one transect to appear ‘laterally-zoned’ and another
340 to appear ‘reverse-zoned’ in terms of Ce-concentration. Bright sector-zones
341 on BSE images are associated with higher Ce-concentrations than dark zones.
342 To gain insight into the variation of clinopyroxene Ce-concentration associ-
343 ated with concentric growth-zonation, transects across grains were averaged
344 *per-experiment*. Ratios of median average Ce-counts / rim Ce-counts repre-
345 sent the difference between the composition of the bulk crystal, as analysed
346 by LA-ICP-MS, and the composition of the clinopyroxene rims that approach
347 chemical equilibrium with the adjacent quenched melt. For the three exper-
348 iments measured, bulk/rim Ce ratios are 1.04 for M3₂, 1.08 for M5 and 1.12
349 for M3 1.25F (from Beard, 2018).

350 In the case of compatible elements, the analyses of bulk crystal trace-
351 element compositions could therefore return apparent partition coefficients
352 that are overestimated by 4–12% relative to equilibrium values. The highest
353 values are found for the largest clinopyroxene crystals and in these, because
354 of their size, we were able to avoid the cores in the analyses via LA-ICP-
355 MS, thereby reducing the growth-zonation bias in apparent trace-element
356 partition-coefficients.

357 Where large clinopyroxene crystals (ca 100 µm) were present and time-
358 averages of element counts could be used for the reduction of laser-ablation
359 data, trace-element-compositions are similar among clinopyroxene crystals
360 within individual experiments indicating that trace-element concentrations
361 in the melt phase remained spatially homogeneous throughout the duration
362 of the experiments (Table S1). Typical trace-element concentrations in the
363 experiment clinopyroxene are illustrated in Supplementary Figure S5c.

364 **5. Discussion**

365 *5.1. Attainment of equilibrium in the Canary Islands rocks*

366 The Canary Islands trace-element partition-coefficients presented here
367 were determined from euhedral, blade-shaped crystals free of melt inclu-
368 sions and chemical zonation. The corresponding quenched melt was in direct
369 contact with these crystals and shows no zonation in backscattered electron
370 images (Fig. 1). While equilibrium conditions are challenging to confirm for
371 a natural volcanic system, the euhedral forms, chemical homogeneity of crys-
372 tals, and congruency between samples from separate eruptions suggest that
373 the crystals grew in a stable environment, and were not subject to chemical
374 or physical perturbations during growth (Fig. 6). In the case of these Ca-
375 nary Islands clinopyroxene, the entire mineral is interpreted to be in chemical
376 equilibrium with the adhered quenched melt.

377 *5.2. Chemical heterogeneity and approach toward equilibrium during the ex-
378 periments*

379 During our experiments crystals of clinopyroxene were grown directly
380 from unseeded glasses and the run temperature was approached from su-
381 perliquidus. No attempts were made to reverse these experiments by re-
382 equilibrating crystals and liquids with deliberately mismatched trace-element
383 concentrations because of sluggish diffusion of most elements through the
384 clinopyroxene structure (Van Orman et al., 2001; Cherniak and Dimanov,
385 2010). Some consideration is therefore required before the proximity to chem-
386 ical equilibrium can be established. Further information on the equilibration
387 of these experiments is in Section 9.

388 A necessary condition for equilibrium is chemical homogeneity within
389 all measured phases. Except for some sector and concentric zonation within
390 clinopyroxene, major- and trace-element concentrations are generally uniform
391 in both the quenched melt and the mineral phases. One potential source
392 of chemical heterogeneity of trace elements is their slow diffusion through
393 clinopyroxene. We now examine this potential effect which could modify our
394 derived partition coefficients.

395 We quantify the departure of apparent partition coefficients from chemi-
396 cal equilibrium with Ce-transects measured across some experiment clinopy-
397 roxene via EPMA, with Ce as a proxy for the other compatible elements
398 (Supplement S1). Concentric growth-zoning has a smaller effect on clinopy-
399 roxene Ce-concentration than sector zoning, the latter of which was can-
400 celled by averaging transects across several grains per experiment. Apparent
401 clinopyroxene–melt partition coefficients for compatible elements (median
402 Ce) are offset from equilibrium (rim Ce) to higher values by 4–8% (Sup-
403 plement S1). Large systematic errors outside of these figures are unlikely
404 because sets of trace-element partition-coefficients of common valence define
405 Ounma parabolae, discounting the presence of melt-inclusions within the
406 experiment clinopyroxene (see Fig. 9 below and Kennedy et al., 1993).

407 A 4–8% systematic positive bias in compatible element partition coef-
408 ficients is small relative to the variation in apparent partition coefficients
409 within our sample set, as well as within literature values. Furthermore,
410 many of our experimentally-derived partition coefficients define trends with
411 clinopyroxene major-element composition that are continuous throughout a
412 set of literature data (Fig. 7 below). At low-degrees of crystallisation ap-

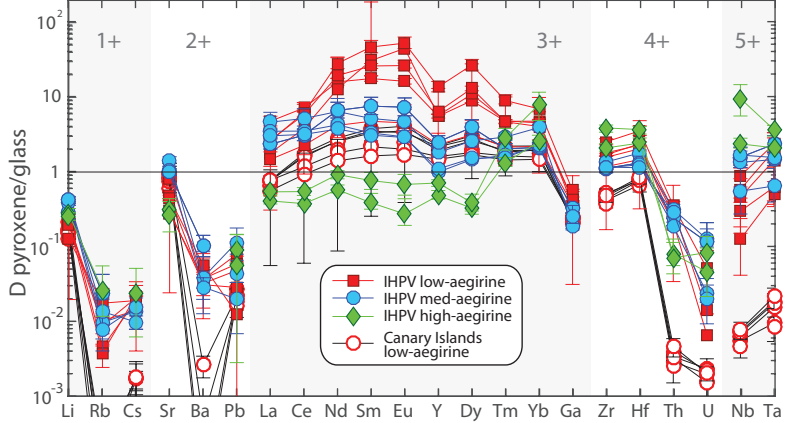


Figure 6: Trace-element partition-coefficients between clinopyroxene and silicate melt, as determined from internally heated pressure vessel experiments ($n = 11$; low-, medium- and high-aegirine types) and from clinopyroxene-rim glass pairs from pyroclastic fall deposits from Tenerife, Canary Islands ($n = 6$; low-aegirine type). Uncertainties on the partition coefficients are at the 1σ level.

413 parent partition coefficients for incompatible elements are more subtly offset
 414 from equilibrium values than those for compatible elements because their
 415 concentration in the melt is more consistent during crystallisation (see sup-
 416 plementary text section 9). Because the potential bias of our apparent par-
 417 tition coefficients is small relative to true equilibrium values no correction
 418 factor has been applied to our data presented in the figures below, or in
 419 Tables 4 and S1.

420 *5.3. Trace-element-partitioning*

421 Apparent trace-element partition-coefficients and their uncertainties were
 422 calculated as mass concentration ratios between clinopyroxene and coex-
 423 isting glass and are reported in Tables 4 and S1. Where trace-element-

concentrations in clinopyroxene could be determined using regular time-averages of counts from the ICP-MS system, a time-weighted average composition of clinopyroxene was used with that of the coexisting glass to calculate apparent trace-element partition-coefficients and their associated uncertainty. Where the laser-ablation unmixing model was required for reduction of clinopyroxene trace-element analyses, the partition coefficients were calculated using time-weighted average compositions of glass alongside the corresponding ‘unmixed’ clinopyroxene trace-element concentration (Supplementary Figure S5). Because a robust-regression data reduction scheme was used, this technique returns a median-average trace-element concentration for clinopyroxene, whilst effectively rejecting outlier data, for example from the ablation of minerals other than clinopyroxene that may have been hidden below the polished surfaces of the grain mounts. Derived trace-element partition-coefficients are consistent between these two data-reduction methodologies to better than 2σ . Uncertainty calculations are described in the caption for Figure S5.

Three markedly different behaviours of rare earth element partitioning are observed in the experiments (Fig. 6). These depend on the aegirine concentration in the clinopyroxene and match the major-element exchange vector domains discussed above. Low-aegirine experiment clinopyroxene (Ae_{5-25}) prefer the MREE; medium-aegirine clinopyroxene (Ae_{25-50}) show a similar behaviour, save for higher LREE partition coefficients, whereas high-aegirine clinopyroxene (Ae_{55-95}) strongly prefer HREE and show incompatible behaviour for the light and middle REE. The experiment REE partition coefficients are 0.3–53, typically 2–6, with minima for LREE and MREE in

449 high-aegirine clinopyroxene (Fig. 6). Our experimental apparent partition
450 coefficients are about an order of magnitude higher than in most other studies
451 of clinopyroxene-melt element-partitioning that were performed on different
452 bulk compositions (Fig. 7d,e,f), with the exception of high Si systems, such
453 as the Bandelier Tuff (cf. Olin and Wolff, 2010).

454 The Canary Islands clinopyroxene show similar rare-earth-element partitioning-
455 systematics to the low-aegirine experiment clinopyroxene, with absolute val-
456 ues for these partition coefficients of about one order of magnitude lower.

457 The high field-strength elements (HFSE) Zr, Hf, Nb and Ta are compati-
458 ble to slightly incompatible in the experimental clinopyroxene, and typically
459 1–2 orders of magnitude less compatible in the Canary Islands clinopyrox-
460 ene (Fig. 7a,b,c). The HFSE are most compatible in sodic clinopyroxene.
461 Partition coefficients for the large-ion lithophile elements K, Sr, Pb are pos-
462 itively correlated with X_{Na}^{M2} in the low- and medium-aegirine clinopyroxene,
463 but are lower in high-aegirine clinopyroxene (Fig. S6). The Rb, Cs and Ba
464 partition coefficients have a high uncertainty and are maximum estimates
465 owing to low concentrations of these elements in the clinopyroxene, close to
466 the detection limit for analyses by LA-ICP-MS. These data are therefore not
467 discussed further. Lithium is incompatible ($D_{Li} = 0.1$ –0.4) in both Canary
468 Islands and experimental clinopyroxene and, like Sr and Pb, becomes more
469 compatible with increasing aegirine content in the clinopyroxene, plateauing
470 at $X_{Na}^{M2} = 0.4$ and decreasing thereafter (Figs. 7g, S6g). The actinides U
471 and Th show contrasting partitioning behaviour; the former showing no cor-
472 relation with aegirine content in the clinopyroxene, the latter becoming more
473 incompatible with increasing aegirine content (Fig. 7h). The U and Th par-

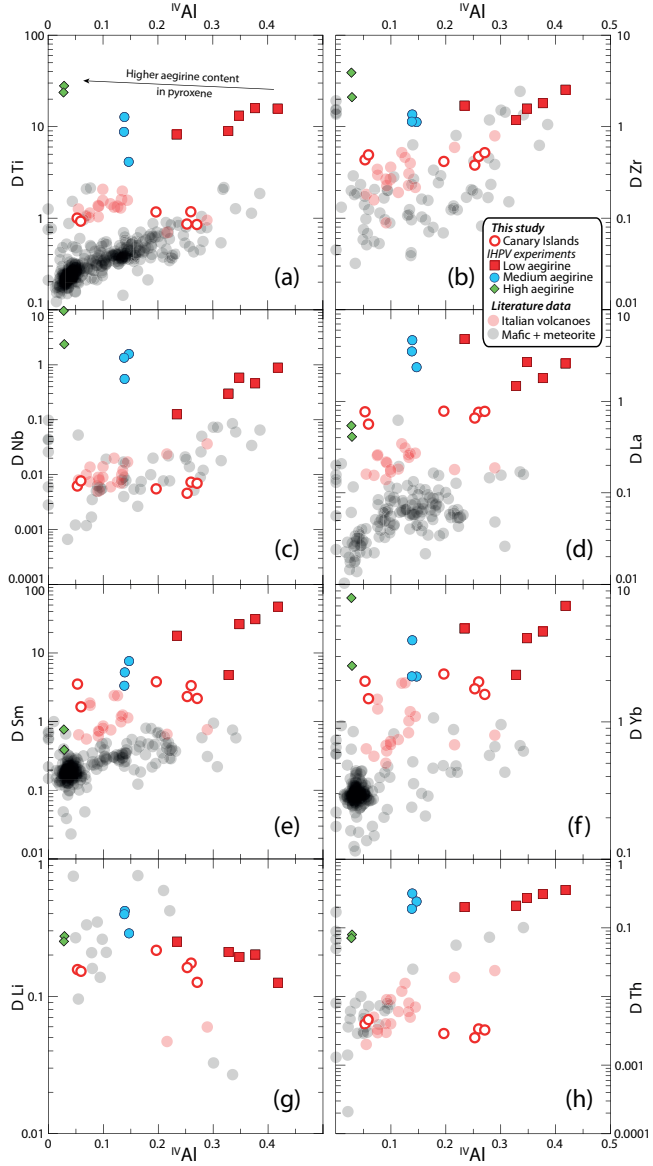


Figure 7: Element partition coefficients for HFSE (Ti, Zr, Nb), REE (La, Sm, Yb) and TE (Li, Th) vs. ^{IV}Al . Literature values ($n = 411$), including those from the Roman Province, Italy, are from the compilation of Bédard (2014), with additional, more recent, data from Mollo et al. (2016). A similar diagram with X_{Na}^{M2} in place of ^{IV}Al is in Supplement S6.

⁴⁷⁴ tition coefficients for our Canary Islands samples are similar to those for the
⁴⁷⁵ Roman Province (Wood and Trigila, 2001; Fedele et al., 2009; Mollo et al.,
⁴⁷⁶ 2013, 2016), and are 1–2 orders of magnitude more incompatible relative to
⁴⁷⁷ the experimental clinopyroxene.

⁴⁷⁸ *5.4. The effects of melt structure on element-partitioning*

⁴⁷⁹ The partitioning of trace-elements between crystals and melts is con-
⁴⁸⁰ trolled by their relative activity in each phase and the exchange mechanisms
⁴⁸¹ by which their incorporation into crystals takes place (e.g., Jd-melt, Jd-DiHd
⁴⁸² and CaTS-DiHd exchanges have been shown to control REE incorporation
⁴⁸³ in cpx, Putirka, 2008; Wood and Blundy, 2014; Mollo et al., 2017). As such,
⁴⁸⁴ one might expect to see correlations between melt structural parameters and
⁴⁸⁵ trace-element-partition coefficients. Such correlations have been reported by
⁴⁸⁶ numerous authors (e.g., Schmidt et al., 2006; Mollo et al., 2017), but appear
⁴⁸⁷ to be expressed over a limited range of melt compositions (Gaetani, 2004;
⁴⁸⁸ Huang et al., 2006). A widely used descriptor for melt structure is the ra-
⁴⁸⁹ tio of non-bonding oxygen anions to tetrahedrally-coordinated cations ($\frac{NBO}{T}$,
⁴⁹⁰ Mysen et al., 1982, 1985). In relatively polymerised melts, where this ratio
⁴⁹¹ falls below 0.49, melt structure has been shown to have a significant influence
⁴⁹² on mineral–melt partition coefficients (Gaetani, 2004; Huang et al., 2006).

⁴⁹³ To calculate NBO/T for our experiments, we estimated melt Fe oxida-
⁴⁹⁴ tion state from run temperatures and known fO_2 buffer conditions (Kress
⁴⁹⁵ and Carmichael, 1991). The recalculated total of major-element oxides (incl.
⁴⁹⁶ Fe_2O_3) was then used to approximate the water content of the quenched
⁴⁹⁷ melts. Oxygen from this dissolved water was added into the NBO/T cal-
⁴⁹⁸ culation, which followed Mysen et al. (1985). The high content of alka-

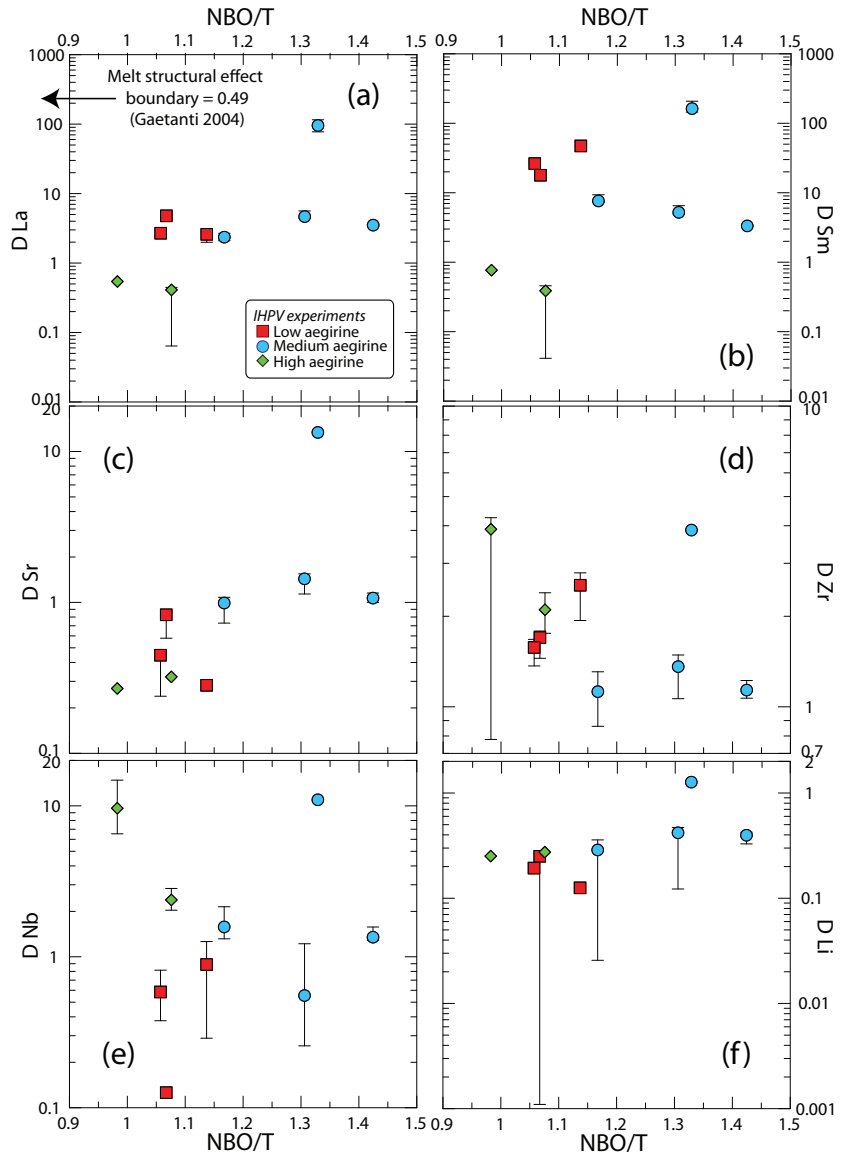


Figure 8: Diagrams of clinopyroxene–melt trace-element-partition coefficients for the IHPV experiments as a function of NBO/T of the quenched melt (Mysen et al., 1985). The water-saturated, sodic compositions investigated produce melts with highly depolymerised structures. The NBO/T ratio of these melts is not correlated with trace-element-partition coefficients, except weakly in the case of Sr. In highly polymerised systems ($\text{NBO}/\text{T} < 0.49$, Gaetani 2004) partition coefficients for REE and HFSE are negatively correlated with this parameter. (see Fig. 9 from Huang et al. 2006).

lies and dissolved water in the experiments presented here produced melts that have NBO/T = 0.98–1.42; well above the compositional boundary reported by Gaetani (2004). Consistent with his findings, most trace-element-partition coefficients determined from our experiments are uncorrelated with the NBO/T ratio of the melt (Fig. 8). An exception is D_{Sr} that shows a weak positive correlation with NBO/T (Fig. 8c). NBO/T could not be calculate for our Canary Islands compositions because the water content of the melt prior to quench is not known.

Because partition coefficients between clinopyroxene and melt are controlled by the relative activity of elements in each of these two phases, an empirical model to predict partition coefficients from both melt and mineral compositional terms has the highest potential for accuracy. Application of such a model would however require measurement of both mineral and melt phases, which would limit its geological utility. A similar model based only on clinopyroxene composition could be applied in a wider range of scenarios where melt composition cannot be directly measured, for example to cumulate systems or to concentrically-zoned phenocrysts. Because crystallisation is a thermodynamically-controlled process, the composition of the melt and thus its effects on element-partitioning will, at least in part, be recorded by the composition of the clinopyroxene. This considered, we chose to calibrate a clinopyroxene-based empirical partitioning model, based on lattice-strain theory that would be applicable over a wide compositional range from tholeiitic basalts to peralkaline phonolites. Details are provided in the following sections.

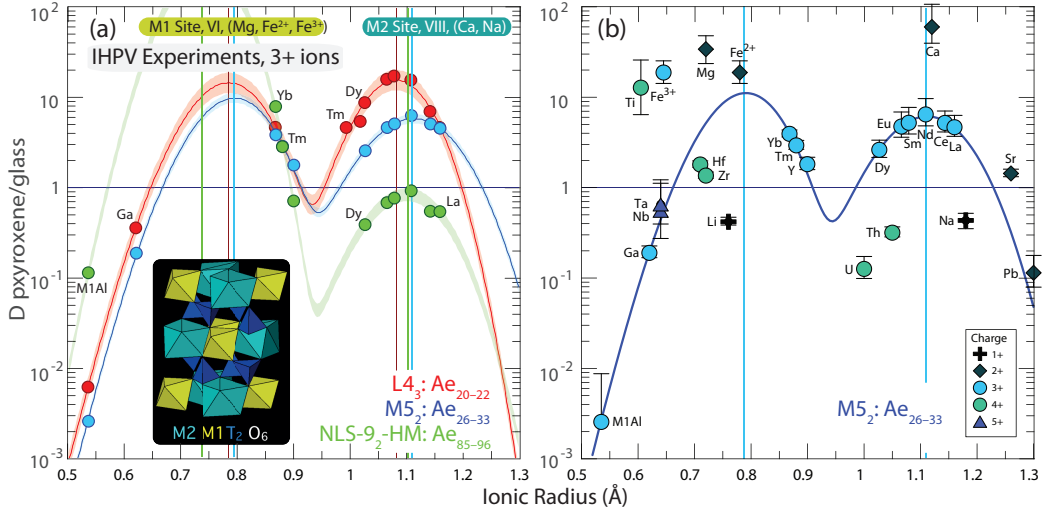


Figure 9: Non-linear weighted least-squares fits to element-partitioning data from the internally heated pressure vessel experiments following the lattice-strain model of Blundy and Wood (1994). (a) Representative fits to 3+ ion partitioning behaviour with examples for low (red), medium (blue) and high-aegirine (green) clinopyroxene experiments. (b) Measured partition coefficients for ions of 1+, 2+, 4+ and 5+ charges that are consistent with the lattice-strain model. Ionic radii are assigned to 6 or 8 fold co-ordination (Shannon, 1976), and were chosen to minimise residuals in the fit (cf. Olin and Wolff, 2010). Y was not included in the fitting routine for 3+ ions because of mass fractionation effects (ibid.). Vertical coloured lines indicate ideal ionic radii (r_0) of M1 and M2 sites and shaded areas indicate 95% confidence intervals on the fits determined via bootstrapping. Uncertainties on the partition coefficients in (b) are 1σ . Fitted lattice-strain parameters are given in Table 4.

523 5.5. Fits to the lattice-strain model

524 The equilibrium partitioning of trace-elements between minerals and melts
 525 is largely controlled by the structure of the crystal lattice, its elasticity (On-
 526 uma et al., 1968; Kumazawa, 1969; Weidner and Vaughan, 1982) and its

527 ability to accommodate an excess or shortage in charge (Blundy et al., 1998;
 528 Wood and Blundy, 2001; Hanchar et al., 2001; Corgne and Wood, 2005). The
 529 lattice-strain model provides a framework in which the influence of these
 530 variables on partitioning behaviour can be quantified, and thus predicted
 531 under conditions bracketed by a calibrating data set (Onuma et al., 1968;
 532 Blundy and Wood, 1994; Wood and Blundy, 2014). The lattice structure of
 533 minerals has a dependence on pressure, temperature and composition, and
 534 element-partitioning is a thermodynamically-controlled process (e.g. Wood
 535 and Blundy, 1997).

536 Most trivalent ions, including the REE and Y enter the M2 site of clinopy-
 537 roxene, which is typically 6- or 8-coordinated (Deer et al., 1992). Smaller
 538 trivalent ions, including Al, Cr, Ga, Sc, and in the case of Fe-rich clinopyrox-
 539 ene the HREE may enter the smaller, octahedral M1 site (Olin and Wolff,
 540 2010; Bédard, 2014). The high field-strength elements Ti, Zr, Hf, Nb and
 541 Ta are typically hosted by the M1 site (Hill et al., 2000, 2011; Dygert et al.,
 542 2014).

543 To investigate systematics in D_i values and the mechanisms by which
 544 trace-elements are incorporated into clinopyroxene, element-partitioning be-
 545 haviour was explored in light of the lattice-strain theory, quantitatively de-
 546 scribed by the lattice-strain equation:

$$D_i^{mineral/melt} = D_0 \exp \left[\frac{-4\pi E_s N_a}{RT} \left(\frac{r_0}{2} (r_0 - r_i)^2 - \frac{1}{3} (r_0 - r_i)^3 \right) \right] \quad (1)$$

547 where r_0 is the ideal radius for the lattice site, E_s is the Young's modulus
 548 (i.e., the lattice site stiffness), D_0 is the strain-free partition coefficient, N_a is
 549 Avagadro's number, R is the gas constant, T is temperature in Kelvin, and

550 r_i is the ionic radius of the element in question, all radii in Å. We focused on
 551 3+ ions that cover a wide range of radii and fitted lattice-strain parameters
 552 for both the M1 and M2 sites of clinopyroxene (Fig. 9):

$$D_i^{cpx/melt} = D_0^{M2} \exp \left[\frac{-4\pi E_s^{M2} N_a}{RT} \left(\frac{r_0^{M2}}{2} (r_0^{M2} - r_i)^2 - \frac{1}{3} (r_0^{M2} - r_i)^3 \right) \right] + D_0^{M1} \exp \left[\frac{-4\pi E_s^{M1} N_a}{RT} \left(\frac{r_0^{M1}}{2} (r_0^{M1} - r_i)^2 - \frac{1}{3} (r_0^{M1} - r_i)^3 \right) \right] \quad (2)$$

553 Parabolae for 3+ ions were fitted for the M1 and M2 sites using the REE, Ga
 554 and Al assigned to the M1 site of clinopyroxene (Fig. 9a). Fits are weighted
 555 based on uncertainties for the element-partition coefficients. HREE have
 556 higher element-partition coefficients than can predicted by substitution into
 557 the M2 site, hence were fitted with ionic radii for sixfold coordination into
 558 the M1 site (*cf.* Olin and Wolff, 2010; Reguir et al., 2012). Lattice-strain
 559 parameters as obtained from fits to the data are shown in Table S1.

560 In some low-aegirine experiments and the Canary Islands rocks, lattice-
 561 strain fitting for 3+ ions at the M1 site was not possible, because too few
 562 HREE partitioned onto the M1 site of these clinopyroxene. Here, we chose
 563 to fit only lattice-strain parameters for the M2 site, or fix D_0^{3+} values for the
 564 M1 site to match those for the M2 site, and fit only the r_0 and E_s parameters
 565 for the M1 site. Fitting of element-partitioning data for 1+, 2+ and 4+ ions
 566 was less successful owing to sparse coverage of suitable radii and detection-
 567 limit issues for some elements. Partition coefficients for 1+, 2+, and 4+
 568 elements follow radius- and charge-dependent trends consistent with lattice-
 569 strain theory and reported effects of charge on lattice-strain parameters (Fig.
 570 9b, e.g., Hazen and Finger, 1979; Law et al., 2000; Adam and Green, 2006).

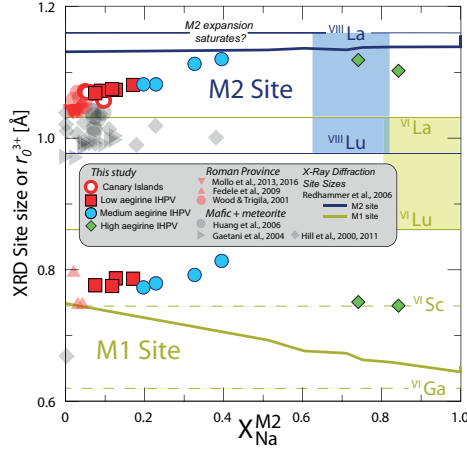


Figure 10: Diagram showing variation of ideal ionic radius r_0^{3+} with X_{Na}^{M2} for M1 and M2 sites of clinopyroxene. Shown for comparison are single crystal x-ray diffraction data from the hedenbergite-aegirine compositional join (heavy solid lines, from Redhammer et al., 2006). Shaded boxes represent the range of ionic radii for rare earth elements in VI and VIII coordination (Shannon, 1976). Literature data for the Roman Province, Italy are from Fedele et al. (2009); Mollo et al. (2013, 2016); Wood and Trigila (2001) and for mafic systems are from Hill et al. (2000, 2011); Gaetani (2004); Huang et al. (2006).

571 *5.5.1. Effects of composition on ideal site size, r_0*

572 As the composition of clinopyroxene shifts from augite toward aegirine,
 573 the size of the M1 and M2 sites, or strain-free radii (r_0), should diverge fol-
 574 lowing the sizes of the major-element cations on these sites. Lattice-strain fits
 575 for 3+ cations indicate expansion of the M2 site between low and medium-
 576 aegirine clinopyroxene, with r_{0M2}^{3+} correlating well with Na replacing Ca (Figs.
 577 9, 10). Expansion of the M2 site stalls at $r_{0M2}^{3+} \approx 1.12 \text{ \AA}$ and $X_{\text{Na}}^{M2} \approx 0.4$,
 578 changing little in size between medium and high-aegirine clinopyroxene. We
 579 suggest that this is a ‘saturation effect’, whereby the smaller ions in the T

and M1 sites prevent further expansion of the M2 site as additional R_{M2}^{+} is added to the clinopyroxene. For the M1 site of clinopyroxene, strain free radii for R^{3+} cations indicate expansion between low and medium-aegirine clinopyroxene and contraction between medium and high-aegirine clinopyroxene (Figs. 9, 10). These trends broadly follow the substitution of Mg^{2+} for Fe^{2+} , then Fe^{2+} for Fe^{3+} with increasing aegirine content in the clinopyroxene.

5.5.2. The effect of cation charge on the D_0 parameter

The D_0 parameter of the lattice-strain model describes ideal, strain-free partitioning and tracks the solubility of an ideal cation in the mineral with changing pressure, temperature and the bulk composition of the system (Wood and Blundy, 2014). D_0 therefore correlates with the major-element composition of the clinopyroxene. Moreover, incorporation of trace-elements of a different charge introduces an electrostatic penalty that leads to a lower D_0 for that charge (Wood and Blundy, 2001, 2003).

The average charge of major-elements on the M2 site of clinopyroxene decreases from 2+ to 1+ on the compositional join between Ca-rich diopside and Na-rich aegirine. Consequently, the electrostatic penalty for substituting a REE³⁺ cation into the clinopyroxene M2 site is increased. Indeed, $D_{0,M2}^{3+}$ decreases as Ca exchanges for Na (Fig. 11e). Conversely, as the average charge on the M1 site of clinopyroxene increases from 2+ toward 3+ in end-member aegirine, the electrostatic penalty incurred when substituting REE³⁺ cations onto the M1 site is reduced (Fig. 11f). As a result, $D_{0,M1}^{3+}$ increases by approximately an order of magnitude between our medium-aegirine and high-aegirine experimental clinopyroxene, an effect that when combined with

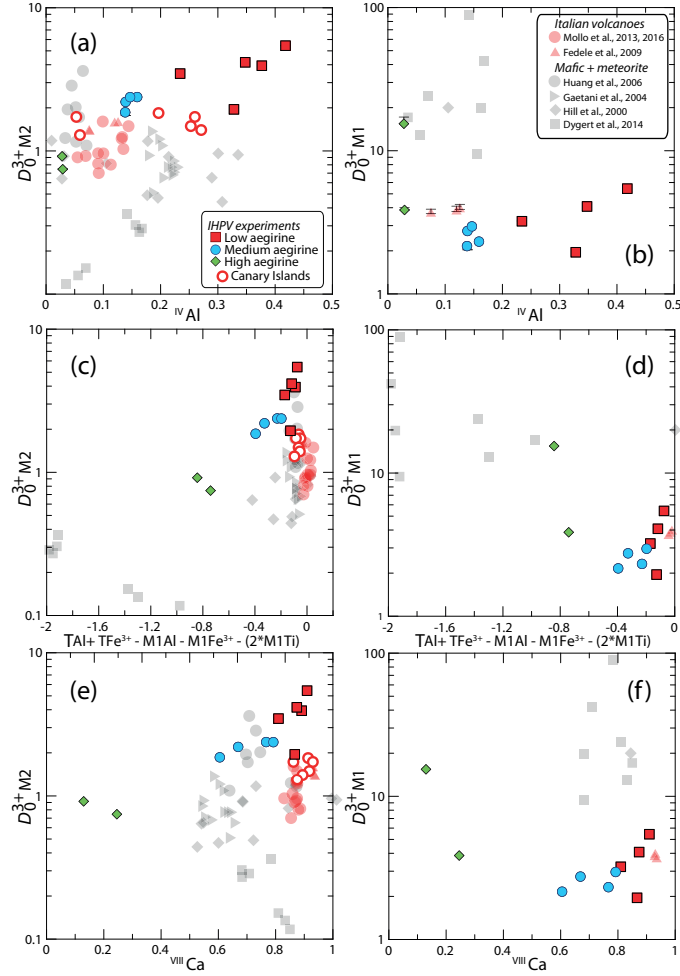


Figure 11: Strain-free partitioning coefficients (D_0) for 3+ ions into clinopyroxene vs. various charge compensation mechanisms. (a,c,e) are for the M2 site, and (b,d,f) are for the M1 site. The diagrams show that variability in partitioning behaviour is highly dependent on mineral composition, and that variation between aegirine-rich clinopyroxene cannot be explained well by the same mechanisms as more mafic systems. Literature data for element-partitioning in Mafic + Meteorite and Roman Province compositions are from the compilation of Bédard (2014). 1σ uncertainties are shown in (a, b) and are usually smaller than the symbol sizes.

605 the shrinking M1 site size, leads to strong fractionation of the HREE (Figs.
606 9 and 11f).

607 A positive correlation between Al^T and partition coefficients for highly
608 charged trace-elements has been extensively documented in studies on clinopy-
609 roxene (Lundstrom et al., 1994; Gaetani and Grove, 1995; Blundy et al., 1998;
610 Francis and Minarik, 2008; Hill et al., 2011; Mollo et al., 2016). The low-
611 aegirine experimental clinopyroxene and most of the Canary Islands rocks ex-
612 tend trends defined by clinopyroxene from mafic systems (Fig. 11a), whereas
613 the remainder of the experimental data set and Canary Islands rocks show
614 element-partitioning behaviour similar to the potassic Roman Province of
615 Italy (Wood and Trigila, 2001; Fedele et al., 2009; Mollo et al., 2016), con-
616 firming that an Al^T -controlled substitution mechanism extends to peralkaline
617 conditions (Figs. 7, 11a).

618 Tetrahedral Al is thought to facilitate incorporation of REE^{3+} cations
619 onto the M2 site of clinopyroxene by replacing Si^{4+} , thereby reducing local
620 charge and thus the electrostatic penalty associated with incorporation of
621 REE (Blundy et al., 1998). The substitution of Fe^{3+} for tetrahedral Si^{4+} can
622 be expected to have a similar effect. Conversely, R^{3+} ions on the neighbouring
623 M1 site should hinder incorporation of REE on the M2 site, because they
624 increase local charge by replacing R^{2+} ions, such as Mg^{2+} and Fe^{2+} . This
625 electrostatic penalty should apply doubly to Ti^{4+} on the M1 site. This effect
626 is consistent with our experimental data (Fig. 11c), but is not obvious in the
627 natural samples, nor in the majority of the literature experimental data. It
628 would thus appear that other factors, such as melt structure, have a stronger
629 control on D_{REE} (e.g. Prowatke and Klemme, 2005).

630 D_0^{3+} parameters for the M1 site are strongly correlated with those for the
631 M2 site, except at aegirine concentrations exceeding 50 mol.%. Similarities to
632 M2 partitioning behaviour likely reflect the dominance of T-site substitution
633 mechanisms in augite clinopyroxene. In the high-aegirine clinopyroxene, T-
634 site substitutions become less important as the T-sites become saturated with
635 Si⁴⁺ (Fig. 5). The replacement of Fe³⁺ at the M1 site by 3+ trace-elements
636 does introduce a charge penalty, therefore D_{0M1}^{3+} increases accordingly.

637 *5.6. An element-partitioning model extending to aegirine clinopyroxene*

638 Partition-coefficients vary systematically with the physiochemical condi-
639 tions of natural and synthetic magmas (cf. Wood and Blundy, 2003). Con-
640 sequently, a host of models have been presented to describe the systematics
641 of element-partitioning between clinopyroxene and silicate melts (Wood and
642 Blundy, 1997, 2001; Hill et al., 2011; Yao et al., 2012; Sun and Liang, 2012;
643 Bédard, 2014; Dygert et al., 2014; Mollo et al., 2016). The majority of these
644 models are based on lattice-strain theory and predict how the lattice param-
645 eters r_0 , E_s , and D_0 vary with composition, temperature and pressure. This
646 semi-thermodynamic approach theoretically permits calculation of partition
647 coefficients for any trace-element, at any set of $P - T - X$ conditions. In
648 reality, all models have a limited working range, as restricted by the input
649 data set. Because existing partitioning models do not reproduce the high
650 $r_{0,M2}^{3+}$ values for clinopyroxene with aegirine contents ≥ 50 mol % (Fig. 12a),
651 they cannot accurately predict REE partitioning behaviour for strongly per-
652 alkaline systems. Here, we present a new empirical model that is calibrated
653 on both our experimental work and natural partition coefficients from Ca-
654 nary Islands rocks, as well as existing partitioning data from the literature

655 (compilation of Bédard, 2014, Fig. 12, Table S1).

656 Our model focuses on the dependence of element-partitioning on clinopy-
657 roxene composition, temperature and pressure only. While partition coeffi-
658 cients are thermodynamically controlled by activity of elements in both the
659 crystal and the melt phase (Wood and Blundy, 2014), and while melt struc-
660 ture has been shown to influence element-partitioning (Huang et al., 2006;
661 Schmidt et al., 2006; Mollo et al., 2017), it is not always possible to measure
662 melt composition directly. For example, equilibrium melt compositions can-
663 not be measured for the cores of zoned clinopyroxene phenocrysts in tephra,
664 or indeed for any crystal from an intrusion in which gravitational segrega-
665 tion of phases has occurred. Therefore, while the predictive power of a model
666 based only on the compositions of the crystal should be lower than that of
667 a model based on both crystal and melt compositions, a crystal-only model
668 may be applied to a wider spectrum of geological scenarios. Melt composi-
669 tion should, at least in part, be recorded by the major-element composition
670 of the clinopyroxene.

671 *5.6.1. The clinopyroxene M2 site*

672 To find the principal physiochemical factors that affect element-partitioning
673 at the M2 site of clinopyroxene, a stepwise least-squares multiple linear re-
674 gression analysis was performed using the lattice-strain parameters r_0^{3+} , E_s^{3+}
675 and D_0^{3+} , temperature, pressure and clinopyroxene composition as inputs.
676 Input parameters were initially examined in binary scatter diagrams to as-
677 certain whether correlations with lattice-strain parameters were linear. If
678 not, interaction compositional terms were added to the initial set of possible
679 fitting parameters that had linear correlations with lattice-strain parameters

680 (e.g. $X_{Al+Fe^{3+}}^T$). Intensive variables for multiple regression models for r_0 ,
681 E_s and D_0 were introduced following a hierarchical forward selection criterion with switching. The largest number of significant terms to describe a
682 lattice-strain parameter was eight for E^{M2} (c.95%, cf. Supplement S4).

684 Because of systematic covariation of compositional parameters in our
685 small data set of experiments and natural samples ($n = 16$), a model cal-
686 ibrated with these points alone would be unable to deconvolve the effects
687 of each major-element on partitioning behaviour. We have therefore added
688 published experiments and natural phenocryst-glass pairs ($n = 75$) to assem-
689 ble a database covering a wide range of composition, pressure, temperature
690 and oxygen fugacity (data from compilation of Bédard 2014, and Mollo et al.
691 2016, 0.0001–3.5 GPa, 650–1345 °C, $\log fO_2 = IW$ to $MH \approx \Delta QFM -5$
692 to +5). clinopyroxene compositions cover XMg 0.031–1, X_{Na}^{M2} 0–0.84 and
693 Al^T 0–0.49 c.f.u. and melt compositions vary widely in terms of Mg# (0–
694 100) and XH_2O (0–0.38). REE partition coefficients also vary significantly
695 (e.g. D_{La} 0.01–4.79; D_{Sm} 0.02–47.24, and D_{Yb} 0.11–8.00). The majority
696 of partition coefficients in the training data set were measured via SIMS
697 or LA-ICP-MS, minimising analytical uncertainty (e.g. from analyses by
698 electron-microprobe).

699 The resultant empirical model accounts well for changes in lattice-strain
700 parameters over a range of compositions from basalt to peralkaline phono-
701 lite, faithfully reproducing large r_0^{M2} values typical for sodic clinopyroxene
702 (Fig. 12, model coefficients in Table 5). Student t-tests show that all of the
703 independent variables included in the models are significant at the 95% con-
704 fidence level and PRESS R^2 values were obtained by repeatedby randomly

705 subsampling the dataset (Stevens, 1996), are close to R^2 values calculated by
 706 regular methods, indicating that the models are robust and have high pre-
 707 dictive power. Full multiple regression reports are available in Supplement
 708 S4. Equations generated by the multiple linear regression calculations are
 709 given below for the M2 site, where a_i are the regression coefficients for the
 710 respective variables:

711

$$\ln D_0^{M2} = a_1 + a_2 T + a_3 X_{Al+Fe^{3+}}^T + a_4 X_{Ti}^{M1} + a_5 X_{Al-Fe^{3+}}^{M1} + a_6 X_{Fe^{2+}}^{M2} \quad (3)$$

$$E^{M2} = a_7 + a_8 P + a_9 X_{Al+Fe^{3+}}^T + a_{10} X_{Al}^{M1} + a_{11} X_{Mg}^{M1} + a_{12} X_{Ti}^{M1} \\ + a_{13} X_{Mg}^{M2} + a_{14} X_{Mg} \quad (4)$$

$$r_0^{M2} = a_{15} + a_{16} T + a_{17} X_{Al-Fe^{3+}}^{M1} + a_{18} X_{Ti}^{M1} + a_{19} X_{Ca}^{M2} + a_{20} X_{Na}^{M2} \quad (5)$$

712 The model for r_0^{M2} is robust with high predictive power and incorporates
 713 compositional controls from the M1 and M2 sites, as well as temperature.
 714 Elevated concentrations of large M2 cations Ca^{2+} and Na^+ are correlated
 715 with large M2 sites. Ti^{4+} cations in the neighbouring M1 site are also cor-
 716 related with expansion of the M2 site, and the concentration of small Al^{3+}
 717 minus larger Fe^{3+} on the M1 site is negatively correlated with r_0^{M2} . The neg-
 718 ative correlation between r_0^{M2} and temperature reflects the sum of changes
 719 to major-element composition that lead to smaller clinopyroxene M2 sites at
 720 higher temperatures. This compositional effect swamps the minor influence
 721 of thermal expansion.

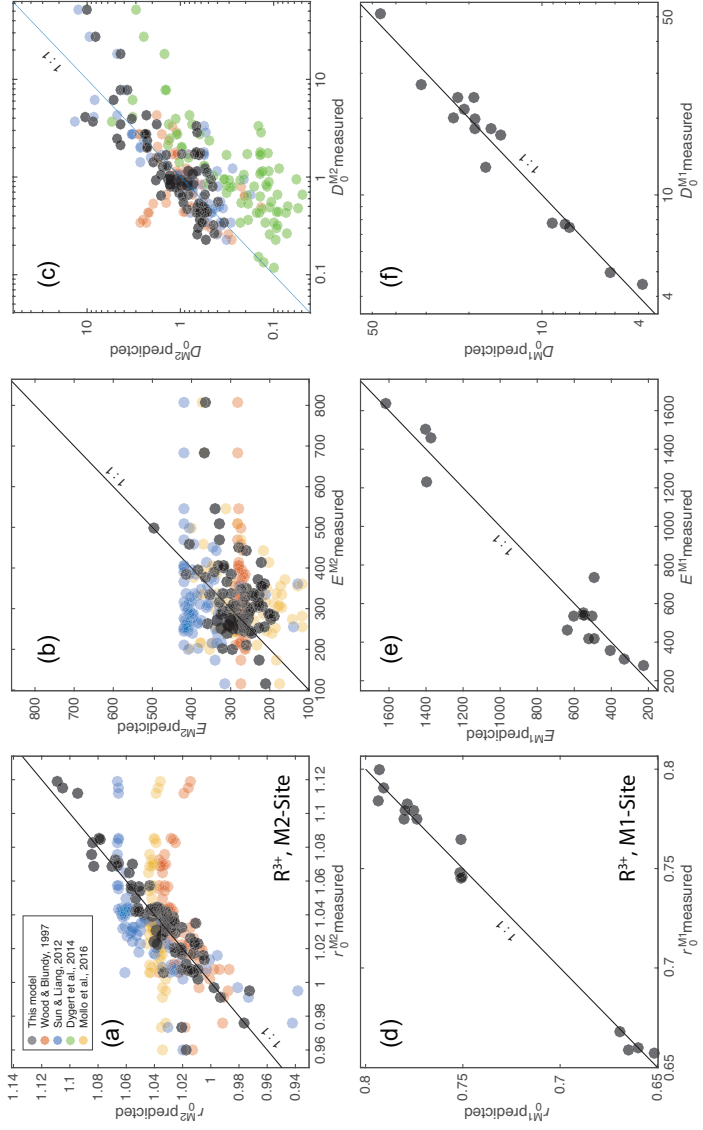


Figure 12: Measured vs. predicted model values for lattice-strain parameters for the M2 and M1 sites of clinopyroxene. The new models presented here were generated via a stepwise multiple linear regression procedure following a hierarchical forward selection criterion with switching. Full regression reports are in Supplement S4 and model equations are in the main text.

722 The model for D_0^{M2} incorporates compositional terms from all three sites
723 in clinopyroxene and temperature. The positive effect of tetrahedral R^{3+}
724 on D_0^{M2} is the largest contribution to the model, which is consistent with
725 published studies (see above). The relationship between clinopyroxene com-
726 positional terms on the M1 and M2 sites and D_0 are indirect and are tied
727 to the solubility of the mineral in the melt (Wood and Blundy, 2003), which
728 in turn is tied to the physiochemical conditions of the system (largely melt
729 composition). The model for D_0^{M2} is less robust than that for r_0^{M2} , largely
730 because there are melt compositional effects that are not recorded in the
731 composition of the clinopyroxene. We tested the Mg# and XH_2O of the
732 melt, neither of which are significant predictors for D_0^{M2} (95% confidence
733 interval).

734 The model for E^{M2} is less well-constrained than for the other two M2
735 lattice-strain parameters, suggesting that M2 site stiffness is not tied strongly
736 to clinopyroxene composition, temperature or pressure. Despite a signifi-
737 cantly lower predictive power, this model still has physical grounding. Stiff-
738 ness of the M2 site is positively correlated with pressure, as might be expected
739 following a simple Hooke's law relationship, and there are some subtle com-
740 positional controls imparted by the T and M1 sites. The poor correlation
741 between E^{M2} , clinopyroxene composition, temperature and pressure is also
742 evident in published element-partitioning models, where E^{M2} is either poorly
743 predicted (Fig. 12b), or set to a fixed value (e.g. Dygert et al., 2014).

744 Diagrams of measured vs. predicted D values for R^{3+} cations are given in
745 Figure 13a, showing the predictive power of the models over a compositional
746 range between basalt and peralkaline phonolite. For the M2 site, 95% of

747 the measured R^{3+} partition coefficients are reproduced within a factor of
 748 ± 2.5 (hard dashed lines), and in extreme cases, the model still reproduces D
 749 values within an order of magnitude, sufficient for the prediction of element-
 750 partitioning trends over a wide range of $P - T - X$. D_{MREE} , such as Sm,
 751 are reproduced more faithfully than D_{LREE} , because their radius is closer to
 752 r_0^{M2} (Fig. 13c,d), and therefore prediction of their partitioning behaviour is
 753 affected less strongly by inaccuracies in predicted E^{M2} values.

754 5.6.2. *The clinopyroxene M1 site*

755 Using a methodology similar to the M2 site, we fitted a predictive model
 756 for partitioning of R^{3+} cations onto the smaller, 6-coordinated M1 site of
 757 clinopyroxene. Lattice-strain parabola were constrained by partitioning data
 758 for Cr, Ga, Sc, and where suitable, the HREE Tm, Yb and Lu (Our IHPV
 759 experiments plus Hill et al. 2000; Fedele et al. 2009; Mollo et al. 2013; Dygert
 760 et al. 2014). The training data set for the M1 site partitioning model is
 761 small relative to that for the M2 site ($n = 18$), and because it is strongly
 762 skewed toward alkaline compositions, it has lower predictive power and is
 763 not recommended for application to mafic magmatic systems. Equations for
 764 the M1 site lattice-strain parameters, as generated by multiple linear least
 765 squares regression, are given below and shown in Figure 12 where b_i are the
 766 regression coefficients (Table 5) for the respective variables:

$$\ln D_0^{M1} = b_1 + b_2 X_{Al}^T + b_3 X_{Fe^{2+}}^{M1} + b_4 X_{Ca}^{M2} + b_5 X_{Na}^{M2} \quad (6)$$

$$E^{M1} = b_6 + b_7 T + b_8 P + b_9 X_{Mg}^{M1} \quad (7)$$

$$r_0^{M1} = b_{10} + b_{11}P + b_{12}X_{Mg}^{M2} + b_{13}X_{Fe^{3+}}^{M1} + b_{14}X_{Ca}^{M2} \quad (8)$$

767 The model for r_0^{M1} is robust and accurately reproduces the input data
 768 set. A negative pressure term may reflect compressional strain on the crystal
 769 lattice. Large Fe^{3+} cations have a positive effect on the size of the M1 site,
 770 while smaller Mg^{2+} cations on the neighbouring M2 site have a negative effect
 771 on M1 site size. The small negative X_{Ca}^{M2} term is indirectly related to the
 772 size of the M1 site.

773 E^{M1} is predicted more accurately than E^{M2} and is largely described by
 774 variations in temperature and pressure. Much like the M2 site, stiffness of
 775 the M1 site appears to be controlled dominantly by physicochemical factors
 776 that are not recorded in the composition of the clinopyroxene.

777 The model for D_0^{M1} contains compositional terms from all three crystal-
 778 lographic sites in clinopyroxene. X_{Al}^T has a strong positive correlation with
 779 D_0^{M1} , consistent with a charge compensation mechanism that aids incorpora-
 780 tion of R^{3+} cations, while terms for M1 and M2 site cations may be indirectly
 781 recording melt compositional effects. Because D_0^{M1} is unusually high for our
 782 high-aegirine experiments, they had to be excluded from the fitting procedure
 783 to permit model convergence. The models for r_0^{M1} and E^{M1} are calibrated
 784 for use all the way to end-member aegirine, but this was not possible for the
 785 D_0^{M1} term, which is calibrated for use up to $\sim Ae_{50}$. Further experiments
 786 at conditions between those that generated our medium and high-aegirine
 787 clinopyroxene would be required to better constrain the clinopyroxene com-
 788 positional record of D_0^{M1} in strongly peralkaline Fe-rich magmas.

789 When applied to our experimental data, and the compilation of partition

790 coefficients from the Roman Province (Fedele et al., 2009; Mollo et al., 2013,
791 2016), the M1 stepwise model reproduces element-partitioning data to a fac-
792 tor of $\frac{+7}{-11}$ at the 95% confidence interval (Fig. 13b). Full regression reports
793 are provided in Supplement S4.

794 For convenience, we provide an EXCEL spreadsheet for calculation of
795 clinopyroxene-melt element-partition coefficients for any trace-element of 3+
796 valence that is large enough to fit onto the M1 or M2 sites of clinopyroxene
797 (Supplement S5). To assess the utility of the partitioning models and to
798 monitor for potential introduction of radius-dependent bias, we show pre-
799 dicted REE patterns normalised to measured ratios for some literature data
800 and our internally heated pressure vessel experiments (Fig. 14). The model
801 accurately reproduces REE patterns at all compositions, except for HREE
802 on the M1 site of clinopyroxene at aegirine contents exceeding \sim 50 mol %
803 (NLS experiments).

804 *5.7. Implications for formation of REE deposits in evolved alkaline intrusions*

805 The solubility of REE and HFSE minerals is strongly enhanced in peral-
806 kaline melts (Watson, 1979; Linnen and Keppler, 1997; Boehnke et al., 2013;
807 Aseri et al., 2015), thus the high concentration of these elements in peralka-
808 line systems may (partially) reflect this fact (Dostal, 2017). Melts containing
809 high concentrations of REE and HFSE are thought to be generated through
810 low degrees of partial melting in the source, followed by residual enrichment
811 during protracted fractional crystallisation (Marks and Markl, 2017). The
812 budget of REE and HFSE in a fractionating magma is influenced by the
813 mineralogy of the crystallising assemblage, and the extent to which these
814 elements are incorporated at minor or trace concentrations.

815 Clinopyroxene is a major ferromagnesian phase that is commonly satu-
816 rated throughout the entire differentiation histories of peralkaline magmatic
817 systems (Ablay et al., 1998; Marks and Markl, 2001; Möller and Williams-
818 Jones, 2016). The composition of the fractionating clinopyroxene has a major
819 impact on the absolute REE concentrations and REE pattern of the residual
820 melt, and ultimately on the ability of a system to develop economic con-
821 centrations of the REE (Fig. 15, e.g. Kogarko, 1990; Sørensen, 1992; Marks
822 et al., 2011). Clinopyroxene in alkaline magmatic systems is initially cal-
823 cic for mafic melts, and becomes increasingly sodic as crystal fractionation
824 proceeds (Marks et al., 2004). Although the REE are compatible in the
825 majority of our experimentally generated clinopyroxene, those approaching
826 aegirine end-member composition, as found in evolved alkaline magmatic
827 systems have the lowest D_{REE} values (Fig. 6). Strongly alkaline magmatic
828 systems are thought to crystallise abundant Ca-pyroxene early in their evolu-
829 tion which may deplete residual liquids with respect to REEs. Consequently,
830 even though crystallisation of Na-pyroxene could enrich residual liquids with
831 REE, the resultant concentration of these metals in the melt would remain
832 low. However, clinopyroxene is not the only phase to crystallise from alkaline
833 magmas, and the majority of additional silicate phases, such as olivine, bi-
834 otite and feldspar have $D_{REE} << 1$, typically 1-4 orders of magnitude lower
835 than clinopyroxene (Larsen, 1979; Kovalenko et al., 1988; Mahood and Sti-
836 mac, 1990; Fedele et al., 2015). Consequently, if the mode of clinopyroxene
837 is low enough, the bulk D_{REE} of the crystallising assemblage would remain
838 below unity, allowing the REE to become enriched in the residual silicate
839 melt.

840 To give insight into the optimum conditions for residual magmatic en-
841 richment of the REE in alkaline systems we modelled the evolution of REE
842 concentrations in the melt during fractional crystallisation of a nepheline
843 syenite body (Fig. 15). Phase relation data and clinopyroxene compositions
844 are from the experimental study of Giehl et al. (2013). Their starting com-
845 position, based on the MiKa dyke, from the Gardar Province, Greenland, is
846 already extremely evolved, with $Mg\# = 2$, $(Na + K)/Al = 1.44$ and $FeO^* = 12$ wt.%.

847 In these models, crystallisation under water-bearing, oxidising conditions
848 produces a high fraction of clinopyroxene that depletes residual melts with
849 respect to Sm, while subtly enriching La. Dry conditions promote abun-
850 dant alkali feldspar (Afs) crystallisation, which effectively enriches the REE
851 content of residual melts. Under oxidising, dry conditions, the La/Sm ra-
852 tio of the residual melt increases with fractionation, because Sm is more
853 effectively incorporated into clinopyroxene. Residual enrichment is most ef-
854 fective under dry, reducing conditions because of a relatively lower fraction
855 of clinopyroxene within the crystallising assemblage. Because of this, the
856 REE enrichment path of the residual melt is close to that of ideal Rayleigh
857 fractionation. Under these reducing, dry conditions and at a temperature of
858 750°C, the experiments of Giehl et al. (2013) attained a crystal fraction of
859 0.8. Here, residual melts would have and 3.2 times La concentration and 2
860 times the Sm concentration relative to their starting composition.

862 Considering these mechanisms, alongside our experimental and Canary
863 Islands data, the best systems to develop high REE concentrations are those
864 that would produce small proportions of Ca-pyroxene early in their crystalli-

sation histories, quickly evolving to more sodic compositions that crystallise aegirine clinopyroxene. Cooling under low-pressure, dry, reducing conditions produces abundant alkali feldspar that in the case of a peralkaline composition, would serve to further increase the alkalinity of the residual melt. Low-degrees of source melting would produce primary melts with (1) high REE concentrations and (2) low melt Mg + Fe, and low modal abundance of clinopyroxene, which would aid enrichment in residual melts via fractional crystallisation.

The HREE-rich nature of peralkaline magmatic systems, both granites and nepheline syenites, is compatible with fractionation of moderately sodic clinopyroxene that have high D_{LREE}/D_{HREE} (e.g. Möller and Williams-Jones, 2016; Dostal, 2017). As crystal fractionation progresses and clinopyroxene compositions evolve toward the aegirine end-member composition, D_{LREE}/D_{HREE} decreases (Fig. 6). This systematic change in element-partitioning behaviour would result in strong HREE enrichment in aegirine-pyroxene cumulates, and would enrich the residual melt with respect to LREE-MREE.

Conclusions

- Our experiments reveal three distinct element-partitioning behaviours for Na-rich clinopyroxene that depend on aegirine content. Each of these is associated with a distinct major-element exchange vector. We do not have the compositional resolution to know if the transition between these behaviours is smooth or step-like.
- Fits to the lattice-strain model of Blundy and Wood (1994) indicate

889 expansion of the M2 site with increasing $\text{Na}_{\text{M}2}^{+}$, to a maximum $r_{0,\text{M}2}^{3+}$ of
890 1.12 Å at $\text{Na}_{\text{M}2}^{+} = 0.4$ c.f.u. Further expansion did not occur at higher
891 Na contents.

- 892 • Both the M1 and M2 sites of clinopyroxene shrink at high-aegirine
893 contents in response to increasing $\sum \text{R}_{\text{M}1}^{3+}$.
- 894 • Charge effects lead to a progressive increase in $D_0^{\text{M}1}$ at the expense
895 of $D_0^{\text{M}2}$, as the exchanges Ca^{2+} for Na^{+} and M^{2+} for Fe^{3+} take place.
896 Much like in systems of lower alkalinity, REE incorporation into clinopy-
897 roxene is dominated by coupled Al–Si substitutions at the T-site.
- 898 • Existing predictive models for clinopyroxene/melt element-partitioning
899 do not accurately reproduce the large M2 site ($r_{0,\text{M}2}^{3+}$) of clinopyroxene
900 with aegirine content exceeding 50 mol%. We have calibrated a new
901 empirical model that may be applied to any composition between basalt
902 and peralkaline phonolite, based on our data from experiments and
903 natural systems, as well as a large compilation of partition coefficients
904 from the literature.
- 905 • Crystallisation of abundant Ca-Mg rich clinopyroxene depletes the resid-
906 ual melts of REE, and inhibits or terminates orthomagmatic enrich-
907 ment processes.
- 908 • Clinopyroxene–melt REE partitioning systematics suggest that nepheline
909 syenites which host REE deposits must originate from low-degree melts
910 with sufficient alkali enrichment to saturate clinopyroxene similar to
911 our medium-aegirine clinopyroxene (Ae_{25-50}). Fractionation of such

912 clinopyroxene enriches residual melts with respect to the HREE, in
913 accord with the composition of REE-mineralised nepheline syenite sys-
914 tems.

915 **Acknowledgements**

916 We thank the Geo.X partners GFZ and Universität Potsdam for access
917 to the HP-GeoMatS Lab, Don Baker for assistance with preparation of start-
918 ing materials, Bruce Watson and Volker Möller for providing samples of Mud
919 Tank zircon and the Nechalacho Layered Suite rocks, respectively, Hans Peter
920 Nabein, Maria Stuff and Julia Pohlenz for assistance with HP experimental
921 equipment, Toby Soutar for help with preparation of the Canary Islands
922 samples, Lang Shi and Glenn Poirier for assistance with electron-microprobe
923 analyses, and Anna Jung for assistance with laser ICP-MS analyses. The
924 manuscript benefited from discussions with Longbo Yang, Rebecca Paisley,
925 Stephan Kolzenburg, Shane Rooyakkers and Jean Bédard. Silvio Mollo,
926 Lorenzo Fedele and an anonymous reviewer are thanked for their insight-
927 ful feedback. Nelson Eby is thanked for editorial handling. This work was
928 funded by PhD scholarships to C.B. from Geotop, DIVEX, and the SEG
929 Canada Foundation, and operating grants to V.vH. and J.S. from the Nat-
930 ural Sciences and Engineering Research Council of Canada (grant numbers
931 RGPIN-2014-05955, RGPAS-462335-2014) and the FQRNT team research
932 project program.

933 **References**

- 934 Ablay, G.J., Carroll, M.R., Palmer, M.R., Martí, J., Sparks, R.S.J.,
935 1998. Basanite–phonolite lineages of the Teide–Pico Viejo volcanic
936 complex, Tenerife, Canary Islands. *Journal of Petrology* 39, 905–936.
937 doi:10.1093/petroj/39.5.905.
- 938 Ablay, G.J., Ernst, G.G.J., Marti, J., Sparks, R.S.J., 1995. The 2 ka sub-
939 plinian eruption of Montaña Blanca, Tenerife. *Bulletin of Volcanology* 57,
940 337–355. doi:10.1007/BF00301292.
- 941 Adam, J., Green, T., 2006. Trace element partitioning between mica- and
942 amphibole-bearing garnet lherzolite and hydrous basanitic melt: 1. Exper-
943 imental results and the investigation of controls on partitioning behaviour.
944 Contributions to Mineralogy and Petrology 152, 1–17. doi:10.1007/s00410-
945 006-0085-4.
- 946 Akasaka, M., Onuma, K., 1980. The join $\text{CaMgSi}_2\text{O}_6$ - $\text{CaFeAlSi}_2\text{O}_6$ -
947 $\text{CaTiAl}_2\text{O}_6$ and its bearing on the Ti-rich fassaitic pyroxenes. Contribu-
948 tions to Mineralogy and Petrology 71, 301–312. doi:10.1007/BF00371672.
- 949 Albert, H., Costa, F., Martí, J., 2015. Timing of magmatic processes and
950 unrest associated with mafic historical monogenetic eruptions in Tenerife
951 Island. *Journal of Petrology* 56, 1945–1966. doi:10.1093/petrology/egv058.
- 952 Andújar, J., Scaillet, B., 2012. Experimental constraints on parameters con-
953 trolling the difference in the eruptive dynamics of phonolitic magmas: the
954 case of Tenerife (Canary Islands). *Journal of Petrology* 53, 1777–1806.
955 doi:10.1093/petrology/egs033.

- 956 Aseri, A.A., Linnen, R.L., Che, X.D., Thibault, Y., Holtz, F., 2015. Effects of
957 fluorine on the solubilities of Nb, Ta, Zr and Hf minerals in highly fluxed
958 water-saturated haplogranitic melts. *Ore Geology Reviews* 64, 736–746.
959 doi:10.1016/j.oregeorev.2014.02.014.
- 960 Beard, C.D., 2018. Mineral-melt trace element partitioning in alkaline mag-
961 matic systems. Phd thesis. McGill University, Montreal, Canada.
- 962 Bédard, J.H., 2014. Parameterizations of calcic clinopyroxene - Melt trace
963 element partition coefficients. *Geochemistry, Geophysics, Geosystems* 15,
964 303–336. doi:10.1002/2013GC005112.
- 965 Behrens, H., Hahn, M., 2009. Trace element diffusion and viscous flow in
966 potassium-rich trachytic and phonolitic melts. *Chemical Geology* 259, 63–
967 77. doi:10.1016/j.chemgeo.2008.10.014.
- 968 Berndt, J., Liebske, C., Holtz, F., Freise, M., Nowak, M., Ziegenbein,
969 D., Hurkuck, W., Koepke, J., 2002. A combined rapid-quench and H₂-
970 membrane setup for internally heated pressure vessels: description and
971 application for water solubility in basaltic melts. *American Mineralogist*
972 87, 1717–1726. doi:10.1029/JB089iB10p08540.
- 973 Blundy, J., Wood, B., 1994. Prediction of crystal–melt partition coefficients
974 from elastic moduli. *Nature* 372, 452–454. doi:10.1038/372452a0.
- 975 Blundy, J.D., Robinson, J.A.C., Wood, B.J., 1998. Heavy REE are compat-
976 ible in clinopyroxene on the spinel lherzolite solidus. *Earth and Planetary
977 Science Letters* 160, 493–504. doi:10.1016/S0012-821X(98)00106-X.

- 978 Boehnke, P., Watson, E.B., Trail, D., Harrison, T.M., Schmitt, A.K.,
979 2013. Zircon saturation re-revisited. *Chemical Geology* 351, 324–334.
980 doi:10.1016/j.chemgeo.2013.05.028.
- 981 Borchert, M., Wilke, M., Schmidt, C., Cauzid, J., Tucoulou, R., 2010. Par-
982 titioning of Ba, La, Yb and Y between haplogranitic melts and aque-
983 ous solutions: An experimental study. *Chemical Geology* 276, 225–240.
984 doi:10.1016/j.chemgeo.2010.06.009.
- 985 Boudreau, A.E., 2004. PALLADIUM, a program to model the chromato-
986 graphic separation of the platinum-group elements, base metals and sulfur
987 in a solidifying pile of igneous crystals. *Canadian Mineralogist* 42, 393–403.
988 doi:10.2113/gscanmin.42.2.393.
- 989 Brown, R.J., Barry, T.L., Branney, M.J., Pringle, M.S., Bryan, S.E., 2003.
990 The Quaternary pyroclastic succession of southeast Tenerife, Canary Is-
991 lands: explosive eruptions, related caldera subsidence, and sector collapse.
992 *Geological Magazine* 140, 265–288. doi:10.1017/S0016756802007252.
- 993 Bryan, S.E., Martí, J., Cas, R.A.F., 1998. Stratigraphy of the Bandas del
994 Sur Formation: an extracaldera record of Quaternary phonolitic explo-
995 sive eruptions from the Las Cañadas edifice, Tenerife (Canary Islands).
996 *Geological Magazine* 135, 605–636. doi:null.
- 997 Carracedo, J.C., Badiola, E.R., Guillou, H., Paterne, M., Scaillet, S.,
998 Torrado, F.J.P., Paris, R., Fra-Paleo, U., Hansen, A., 2007. Eruptive
999 and structural history of Teide Volcano and rift zones of Tenerife, Ca-

- 1000 nary Islands. Geological Society of America Bulletin 119, 1027–1051.
1001 doi:10.1130/B26087.1.
- 1002 Carroll, M.R., Blank, J.G., 1997. The solubility of H₂O in phonolitic melts.
1003 American Mineralogist 82, 549–556. doi:10.1093/petrology/32.5.1021.
- 1004 Cherniak, D.J., Dimanov, A., 2010. Diffusion in pyroxene, mica and
1005 amphibole. Reviews in Mineralogy and Geochemistry 72, 641–690.
1006 doi:10.2138/rmg.2010.72.14.
- 1007 Chou, I.M., 1986. Permeability of precious metals to hydrogen at 2 kb total
1008 pressure and elevated temperatures. American Journal of Science 286,
1009 638–658.
- 1010 Corgne, A., Wood, B.J., 2005. Trace element partitioning and substitu-
1011 tion mechanisms in calcium perovskites. Contributions to Mineralogy and
1012 Petrology 149, 85–97. doi:10.1007/s00410-004-0638-3.
- 1013 Costa, F., Chakraborty, S., Dohmen, R., 2003. Diffusion coupling between
1014 major and trace elements and a model for the calculation of magma cham-
1015 ber residence times using plagioclase. Geochimica et Cosmochimica Acta
1016 67, 2189–2200. doi:10.1016/S0016-7037(00)01345-5.
- 1017 Coumans, J.P., Stix, J., Clague, D.A., Minarik, W.G., Layne, G.D., 2016.
1018 Melt-rock interaction near the Moho: Evidence from crystal cargo in lavas
1019 from near-ridge seamounts. Geochimica et Cosmochimica Acta 191, 139–
1020 164. doi:10.1016/j.gca.2016.07.017.
- 1021 Deer, W.A., Howie, R.A., Zussman, J., 1992. An introduction to the rock-
1022 forming minerals. Longman Group Ltd, New York.

- 1023 Dostal, J., 2017. Rare earth element deposits of alkaline igneous rocks. *Re-*
1024 *sources* 6, 1–12. doi:10.3390/resources6030034.
- 1025 Downes, H., Balaganskaya, E., Beard, A., Liferovich, R., Demaiffe, D.,
1026 2005. Petrogenetic processes in the ultramafic, alkaline and carbonatitic
1027 magmatism in the Kola Alkaline Province: A review. *Lithos* 85, 48–75.
1028 doi:10.1016/j.lithos.2005.03.020.
- 1029 Droop, G.T.R., 1987. A general equation for estimating Fe³⁺ concentrations
1030 in ferromagnesian silicates and oxides from microprobe analyses, using
1031 stoichiometric criteria. *Mineralogical magazine* 51, 431–435.
- 1032 Dygert, N., Liang, Y., Sun, C., Hess, P., 2014. An experimental study of
1033 trace element partitioning between augite and Fe-rich basalts. *Geochimica
et Cosmochimica Acta* 132, 170–186. doi:10.1016/j.gca.2014.01.042.
- 1035 Edgar, C.J., Wolff, J.A., Olin, P.H., Nichols, H.J., Pittari, A., Cas, R.A.F.,
1036 Reiners, P.W., Spell, T.L., Martí, J., 2007. The late Quaternary Diego Her-
1037 nandez Formation, Tenerife: Volcanology of a complex cycle of voluminous
1038 explosive phonolitic eruptions. *Journal of Volcanology and Geothermal Re-
1039 search* 160, 59–85. doi:10.1016/j.jvolgeores.2006.06.001.
- 1040 Eugster, H.P., Wones, D.R., 1962. Stability relations of the ferruginous bi-
1041 otite, annite. *Journal of Petrology* 3, 82–125. doi:10.1093/petrology/3.1.82.
- 1042 Fedele, L., Lustrino, M., Melluso, L., Morra, V., Zanetti, A., Van-
1043 nucci, R., 2015. Trace-element partitioning between plagioclase, alkali
1044 feldspar, Ti-magnetite, biotite, apatite, and evolved potassic liquids from

- 1045 Campi Flegrei (Southern Italy). *American Mineralogist* 100, 233–249.
1046 doi:10.2138/am-2015-4995.
- 1047 Fedele, L., Zanetti, A., Morra, V., Lustrino, M., Melluso, L., Vannucci,
1048 R., 2009. Clinopyroxene/liquid trace element partitioning in natural
1049 trachyte–trachyphonolite systems: insights from Campi Flegrei (south-
1050 ern Italy). *Contributions to Mineralogy and Petrology* 158, 337–356.
1051 doi:10.1007/s00410-009-0386-5.
- 1052 Foley, S.F., Prelevic, D., Rehfeldt, T., Jacob, D.E., 2013. Minor and
1053 trace elements in olivines as probes into early igneous and mantle
1054 melting processes. *Earth and Planetary Science Letters* 363, 181–191.
1055 doi:10.1016/j.epsl.2012.11.025.
- 1056 Francis, D., Minarik, W., 2008. Aluminum-dependent trace element parti-
1057 tioning in clinopyroxene. *Contributions to Mineralogy and Petrology* 156,
1058 439–451. doi:10.1007/s00410-008-0295-z.
- 1059 Gaetani, G.A., 2004. The influence of melt structure on trace element par-
1060 titioning near the peridotite solidus. *Contributions to Mineralogy and*
1061 *Petrology* 147, 511–527. doi:10.1007/s00410-004-0575-1.
- 1062 Gaetani, G.A., Grove, T.L., 1995. Partitioning of rare earth elements between
1063 clinopyroxene and silicate melt: Crystal-chemical controls. *Geochimica et*
1064 *Cosmochimica Acta* 59, 1951–1962. doi:10.1016/0016-7037(95)00119-0.
- 1065 Gaillard, F., Scaillet, B., Pichavant, M., 2002. Kinetics of iron oxidation-
1066 reduction in hydrous silicic melts. *American Mineralogist* 87, 829–837.
1067 doi:10.2138/am-2002-0704.

- 1068 Giehl, C., Marks, M., Nowak, M., 2013. Phase relations and liquid lines
1069 of descent of an iron-rich peralkaline phonolitic melt: an experimen-
1070 tal study. Contributions to Mineralogy and Petrology 165, 283–304.
1071 doi:10.1007/s00410-012-0809-6.
- 1072 Giordano, D., Nichols, A., Dingwell, D., 2005. Glass transition temperatures
1073 of natural hydrous melts: a relationship with shear viscosity and impli-
1074 cations for the welding process. Journal of Volcanology and Geothermal
1075 Research 142, 105–118. doi:10.1016/j.jvolgeores.2004.10.015.
- 1076 Girnis, A.V., Bulatov, V.K., Brey, G.P., Gerdes, A., Höfer, H.E., 2013. Trace
1077 element partitioning between mantle minerals and silico-carbonate melts
1078 at 6–12 GPa and applications to mantle metasomatism and kimberlite
1079 genesis. Lithos 160–161, 183–200. doi:10.1016/j.lithos.2012.11.027.
- 1080 Goodenough, K.M., Schilling, J., Jonsson, E., Kalvig, P., Charles, N., Tuduri,
1081 J., Deady, E.A., Sadeghi, M., Schiellerup, H., Müller, A., Bertrand, G.,
1082 Arvanitidis, N., Eliopoulos, D.G., Shaw, R.A., Thrane, K., Keulen, N.,
1083 2016. Europe's rare earth element resource potential: An overview of
1084 REE metallogenetic provinces and their geodynamic setting. Ore Geology
1085 Reviews 72, 838–856. doi:10.1016/j.oregeorev.2015.09.019.
- 1086 Grove, T.L., Baker, M.B., Kinzler, R.J., 1984. Coupled CaAl-NaSi dif-
1087 fusion in plagioclase feldspar: Experiments and applications to cooling
1088 rate speedometry. Geochimica et Cosmochimica Acta 48, 2113–2121.
1089 doi:10.1016/0016-7037(84)90391-0.
- 1090 Guillou, H., Carracedo, J.C., Paris, R., Pérèz Torrado, F.J., 2004. Implica-

- 1091 tions for the early shield-stage evolution of Tenerife from K/Ar ages and
1092 magnetic stratigraphy. *Earth and Planetary Science Letters* 222, 599–614.
1093 doi:10.1016/j.epsl.2004.03.012.
- 1094 Gurenko, A.A., Hoernle, K.A., Hauff, F., Schmincke, H.U., Han, D., Miura,
1095 Y.N., Kaneoka, I., 2006. Major, trace element and NdSrPbOHeAr isotope
1096 signatures of shield stage lavas from the central and western Canary Is-
1097 lands: Insights into mantle and crustal processes. *Chemical Geology* 233,
1098 75–112. doi:10.1016/j.chemgeo.2006.02.016.
- 1099 Hanchar, J.M., Finch, R.J., Hoskin, P.W.O., Watson, E.B., Cher-
1100 niak, D.J., Mariano, A.N., 2001. Rare earth elements in synthetic
1101 zircon: Part 1. Synthesis, and rare earth element and phospho-
1102 rus doping. *American Mineralogist* 86, 667–680. doi:10.1130/0091-
1103 7613(1990)018;0757:CTOGAS;2.3.CO;2.
- 1104 Hazen, R.M., Finger, L.W., 1979. Bulk modulus-volume relationship for
1105 cation-anion polyhedra. *Journal of Geophysical Research: Solid Earth* 84,
1106 6723–6728. doi:10.1029/JB084iB12p06723.
- 1107 Hill, E., Blundy, J.D., Wood, B.J., 2011. Clinopyroxene-melt trace ele-
1108 ment partitioning and the development of a predictive model for HFSE
1109 and Sc. *Contributions to Mineralogy and Petrology* 161, 423–438.
1110 doi:10.1007/s00410-010-0540-0.
- 1111 Hill, E., Wood, B.J., Blundy, J.D., 2000. The effect of Ca-Tschermaks com-
1112 ponent on trace element partitioning between clinopyroxene and silicate
1113 melt. *Lithos* 53, 203–215. doi:10.1016/S0024-4937(00)00025-6.

- 1114 Huang, F., Lundstrom, C.C., McDonough, W.F., 2006. Effect of melt
1115 structure on trace-element partitioning between clinopyroxene and sili-
1116 cic, alkaline, aluminous melts. *American Mineralogist* 91, 1385–1400.
1117 doi:10.2138/am.2006.1909.
- 1118 Jugo, P.J., Wilke, M., Botcharnikov, R.E., 2010. Sulfur K-edge XANES anal-
1119 ysis of natural and synthetic basaltic glasses: Implications for S speciation
1120 and S content as function of oxygen fugacity. *Geochimica et Cosmochimica
1121 Acta* 74, 5926–5938. doi:10.1016/j.gca.2010.07.022.
- 1122 Kennedy, A.K., Lofgren, G.E., Wasserburg, G.J., 1993. An experimental
1123 study of trace element partitioning between olivine, orthopyroxene and
1124 melt in chondrules: equilibrium values and kinetic effects. *Earth and Plan-
1125 etary Science Letters* 115, 177–195. doi:10.1016/0012-821X(93)90221-T.
- 1126 Kogarko, L.N., 1990. Ore-forming potential of alkaline magmas. *Lithos* 26,
1127 167–175. doi:10.1016/0024-4937(90)90046-4.
- 1128 Kovalenko, V.I., Hervig, R.L., Sheridan, M.F., 1988. Ion microprobe anal-
1129 yses of trace elements in anorthoclase, hedenbergite, aenigmatite, quartz,
1130 apatite and glass in pantellerite: evidence for high water contents in pan-
1131 tellerite melt. *American Mineralogist* 73, 1038–1045.
- 1132 Kress, V.C., Carmichael, I.S.E., 1991. The compressibility of silicate liquids
1133 containing Fe₂O₃ and the effect of composition, temperature, oxygen fu-
1134 gacity and pressure on their redox states. *Contributions to Mineralogy and
1135 Petrology* 108, 82–92. doi:10.1007/BF00307328.

- 1136 Kumazawa, M., 1969. The elastic constants of single-crystal or-
1137 thopyroxene. *Journal of Geophysical Research* 74, 5973–5980.
1138 doi:10.1029/JB074i025p05973.
- 1139 Larsen, L.M., 1979. Distribution of REE and other trace elements between
1140 phenocrysts and peralkaline undersaturated magmas, exemplified by rocks
1141 from the Gardar igneous province, south Greenland. *Lithos* 12, 303–315.
1142 doi:10.1016/0024-4937(79)90022-7.
- 1143 Law, K.M., Blundy, J.D., Wood, B.J., Ragnarsdottir, K.V., 2000. Trace ele-
1144 ment partitioning between wollastonite and silicate-carbonate melt. *Min-
1145 eralogical Magazine* 64, 651–661. doi:10.1180/002646100549670.
- 1146 Le Bas, M.J., Le Maitre, R.W., Streckeisen, A., Zanettin, B., 1986. A Chem-
1147 ical Classification of Volcanic Rocks Based on the Total Alkali-Silica Dia-
1148 gram. *Journal of Petrology* 27, 745–750. doi:10.1093/petrology/27.3.745.
- 1149 Liang, Y., Richter, F.M., Watson, E.B., 1994. Convection in multicom-
1150 ponent silicate melts driven by coupled diffusion. *Nature* 369, 390–392.
1151 doi:10.1038/369390a0.
- 1152 Linnen, R.L., Keppler, H., 1997. Columbite solubility in granitic melts:
1153 consequences for the enrichment and fractionation of Nb and Ta in the
1154 Earth's crust. *Contributions to Mineralogy and Petrology* 128, 213–227.
1155 doi:10.1007/s004100050304.
- 1156 Lofgren, G., 1989. Dynamic crystallization of chondrule melts of porphyritic
1157 olivine composition: Textures experimental and natural. *Geochimica et
1158 Cosmochimica Acta* 53, 461–470. doi:10.1016/0016-7037(89)90397-9.

- 1159 Lofgren, G.E., Huss, G.R., Wasserburg, G.J., 2006. An experimental study
1160 of trace-element partitioning between Ti-Al-clinopyroxene and melt: Equi-
1161 librium and kinetic effects including sector zoning. *American Mineralogist*
1162 91, 1596–1606. doi:10.2138/am.2006.2108.
- 1163 Lu, F., Anderson, A.T., Davis, A.M., 1995. Diffusional gradients at the crys-
1164 tal / melt interface and their effect on the compositions of melt inclusions.
1165 *The Journal of Geology* 103, 591–597.
- 1166 Lundstrom, C.C., Shaw, H.F., Ryerson, F.J., Phinney, D.L., Gill, J.B.,
1167 Williams, Q., 1994. Compositional controls on the partitioning of U, Th,
1168 Ba, Pb, Sr and Zr between clinopyroxene and haplobasaltic melts: impli-
1169 cations for uranium series disequilibria in basalts. *Earth and Planetary
1170 Science Letters* 128, 407–423. doi:10.1016/0012-821X(94)90159-7.
- 1171 Mahood, G.A., Stimac, J.A., 1990. Trace-element partitioning in pantel-
1172 lerites and trachytes. *Geochimica et Cosmochimica Acta* 54, 2257–2276.
1173 doi:10.1016/0016-7037(90)90050-U.
- 1174 Marks, M., Halama, R., Wenzel, T., Markl, G., 2004. Trace element vari-
1175 ations in clinopyroxene and amphibole from alkaline to peralkaline syen-
1176 ites and granites: implications for mineral-melt trace-element partitioning.
1177 *Chemical Geology* 211, 185–215. doi:10.1016/j.chemgeo.2004.06.032.
- 1178 Marks, M., Markl, G., 2001. Fractionation and assimilation processes in the
1179 alkaline augite syenite unit of the Ilímaussaq intrusion, south Greenland,
1180 as deduced from phase equilibria. *Journal of Petrology* 42, 1947–1969.
1181 doi:10.1093/petrology/42.10.1947.

- 1182 Marks, M., Markl, G., 2003. Ilímaussaq en miniature': closed-system frac-
1183 tionation in an agpaitic dyke rock from the Gardar Province, South Green-
1184 land (contribution to the mineralogy of Ilímaussaq no. 117). Mineralogical
1185 Magazine 67, 893–919. doi:10.1180/0026461036750150.
- 1186 Marks, M.A., Markl, G., 2017. A global review on agpaitic rocks. Earth-
1187 Science Reviews 173, 229–258. doi:10.1016/j.earscirev.2017.06.002.
- 1188 Marks, M.A.W., Hettmann, K., Schilling, J., Frost, B.R., Markl, G., 2011.
1189 The mineralogical diversity of alkaline igneous rocks: Critical factors for
1190 the transition from miaskitic to agpaitic phase assemblages. Journal of
1191 Petrology 52, 439–455. doi:10.1093/petrology/egq086.
- 1192 Möller, V., Williams-Jones, A.E., 2016. Petrogenesis of the Necho-
1193 lacho Layered Suite, Canada: magmatic Evolution of a REE-Nb-
1194 rich Nepheline Syenite Intrusion. Journal of Petrology 57, 229–276.
1195 doi:10.1093/petrology/egw003.
- 1196 Mollo, S., Blundy, J.D., Giacomoni, P., Nazzari, M., Scarlato, P., Coltorti,
1197 M., Langone, A., Andronico, D., 2017. Clinopyroxene-melt element par-
1198 titioning during interaction between trachybasaltic magma and siliceous
1199 crust: Clues from quartzite enclaves at Mt. Etna volcano. Lithos 284-285,
1200 447–461. doi:10.1016/j.lithos.2017.05.003.
- 1201 Mollo, S., Blundy, J.D., Iezzi, G., Scarlato, P., Langone, A., 2013. The
1202 partitioning of trace elements between clinopyroxene and trachybasaltic
1203 melt during rapid cooling and crystal growth. Contributions to Mineralogy
1204 and Petrology 166, 1633–1654. doi:10.1007/s00410-013-0946-6.

- 1205 Mollo, S., Forni, F., Bachmann, O., Blundy, J.D., De Astis, G., Scarlato,
1206 P., 2016. Trace element partitioning between clinopyroxene and trachy-
1207 phonolitic melts: A case study from the Campanian Ignimbrite (Campi
1208 Flegrei, Italy). *Lithos* 252253, 160–172. doi:10.1016/j.lithos.2016.02.024.
- 1209 Moore, G., Vennemann, T., Carmichael, I.S.E., 1998. An empirical model
1210 for the solubility of H₂O in magmas to 3 kilobars. *American Mineralogist*
1211 83, 36–42. doi:10.1016/0012-821X(73)90129-5.
- 1212 Morimoto, N., 1989. Nomenclature of pyroxenes. *Mineralogical Journal* 14,
1213 198–221. doi:10.2465/minerj.14.198.
- 1214 Mungall, J., Brenan, J., 2014. Partitioning of platinum-group elements and
1215 Au between sulfide liquid and basalt and the origins of mantle-crust frac-
1216 tionation of the chalcophile elements. *Geochimica et Cosmochimica Acta*
1217 125, 265–289. doi:10.1016/j.gca.2013.10.002.
- 1218 Mysen, B.O., Virgo, D., Seifert, F.A., 1982. The structure of silicate melts:
1219 Implications for chemical and physical properties of natural magma. *Re-
1220 views of Geophysics* 20, 353–383. doi:10.1029/RG020i003p00353.
- 1221 Mysen, B.O., Virgo, D., Seifert, F.A., 1985. Relationships between properties
1222 and structure of aluminosilicate melts. *American Mineralogist* 70, 88–105.
1223 doi:10.1007/BF00413348.
- 1224 Niu, Y., 2004. Bulk-rock major and trace element compositions of abyssal
1225 peridotites: Implications for mantle melting, melt extraction and post-
1226 melting processes beneath Mid-Ocean ridges. *Journal of Petrology* 45,
1227 2423–2458. doi:10.1093/petrology/egh068.

- 1228 Olin, P.H., Wolff, J.A., 2010. Rare earth and high field strength element par-
1229 titioning between iron-rich clinopyroxenes and felsic liquids. Contributions
1230 to Mineralogy and Petrology 160, 761–775. doi:10.1007/s00410-010-0506-2.
- 1231 Onuma, N., Higuchi, H., Wakita, H., Nagasawa, H., 1968. Trace element
1232 partition between two pyroxenes and the host lava. Earth and Planetary
1233 Science Letters 5, 47–51. doi:10.1016/S0012-821X(68)80010-X.
- 1234 Paton, C., Hellstrom, J., Paul, B., Woodhead, J., Hergt, J., 2011. Io-
1235 lite: Freeware for the visualisation and processing of mass spectromet-
1236 ric data. Journal of Analytical Atomic Spectrometry 26, 2508–2518.
1237 doi:10.1039/C1JA10172B.
- 1238 Peters, S.T., Troll, V.R., Weis, F.A., Dallai, L., Chadwick, J.P., Schulz, B.,
1239 2017. Amphibole megacrysts as a probe into the deep plumbing system
1240 of Merapi volcano, Central Java, Indonesia. Contributions to Mineralogy
1241 and Petrology 172, 1–20. doi:10.1007/s00410-017-1338-0.
- 1242 Prowatke, S., Klemme, S., 2005. Effect of melt composition on the parti-
1243 tioning of trace elements between titanite and silicate melt. Geochimica
1244 et Cosmochimica Acta 69, 695–709. doi:10.1016/j.gca.2004.06.037.
- 1245 Putirka, K.D., 2008. Thermometers and Barometers for Volcanic
1246 Systems. Reviews in Mineralogy and Geochemistry 69, 61–120.
1247 doi:10.2138/rmg.2008.69.3.
- 1248 Rapp, R.P., Watson, E.B., 1986. Monazite solubility and dissolution ki-
1249 netics: implications for the thorium and light rare earth chemistry of

- 1250 felsic magmas. Contributions to Mineralogy and Petrology 94, 304–316.
1251 doi:10.1007/BF00371439.
- 1252 Rasband, W., 2016. ImageJ, U.S. National Institutes of Health, Bethesda,
1253 Maryland, USA.
- 1254 Redhammer, G.J., Amthauer, G., Roth, G., Tippelt, G., Lotter-
1255 moser, W., 2006. Single-crystal X-ray diffraction and temperature
1256 dependent ^{57}Fe Mössbauer spectroscopy on the hedenbergite-aegirine
1257 $(\text{Ca},\text{Na})(\text{Fe}^{2+},\text{Fe}^{3+})\text{Si}_2\text{O}_6$ solid solution. American Mineralogist 91,
1258 1271–1292. doi:10.2138/am.2006.2173.
- 1259 Reguir, E.P., Chakhmouradian, A.R., Pisiak, L., Halden, N.M., Yang, P.,
1260 Xu, C., Kynický, J., Couëslan, C.G., 2012. Trace-element composition
1261 and zoning in clinopyroxene- and amphibole-group minerals: Implications
1262 for element partitioning and evolution of carbonatites. Lithos 128, 27–45.
1263 doi:10.1016/j.lithos.2011.10.003.
- 1264 Rubatto, D., Hermann, J., 2007. Experimental zircon/melt and
1265 zircon/garnet trace element partitioning and implications for the
1266 geochronology of crustal rocks. Chemical Geology 241, 38–61.
1267 doi:10.1016/j.chemgeo.2007.01.027.
- 1268 Schmidt, B.C., Behrens, H., 2008. Water solubility in phonolite melts: Influ-
1269 ence of melt composition and temperature. Chemical Geology 256, 259–
1270 268. doi:10.1016/j.chemgeo.2008.06.043.
- 1271 Schmidt, K.H., Bottazzi, P., Vannucci, R., Mengel, K., 1999. Trace element
1272 partitioning between phlogopite, clinopyroxene and leucite lamproite melt.

- 1273 Earth and Planetary Science Letters 168, 287–299. doi:10.1016/S0012-
1274 821X(99)00056-4.
- 1275 Schmidt, M.W., Connolly, J.A.D., Günther, D., Bogaerts, M., 2006. Element
1276 partitioning: The role of melt structure and composition. Science 312,
1277 1646–1650. doi:10.1126/science.1126690.
- 1278 Severs, M.J., Beard, J.S., Fedele, L., Hanchar, J.M., Mutchler, S.R., Bodnar,
1279 R.J., 2009. Partitioning behavior of trace elements between dacitic melt
1280 and plagioclase, orthopyroxene, and clinopyroxene based on laser ablation
1281 ICPMS analysis of silicate melt inclusions. Geochimica et Cosmochimica
1282 Acta 73, 2123–2141. doi:10.1016/j.gca.2009.01.009.
- 1283 Shannon, R., 1976. Revised effective ionic radii and systematic studies of
1284 interatomic distances in halides and chalcogenides. Acta Crystallographica
1285 Section A 32, 751–767.
- 1286 Shea, T., Hammer, J.E., 2013. Kinetics of cooling- and decompression-
1287 induced crystallization in hydrous mafic-intermediate magmas.
1288 Journal of Volcanology and Geothermal Research 260, 127–145.
1289 doi:10.1016/j.jvolgeores.2013.04.018.
- 1290 Shearer, C.K., Larsen, L.M., 1994. Sector-zoned aegirine from the Ilmaussaq
1291 alkaline intrusion, South Greenland; implications for trace-element behav-
1292 ior in pyroxene. American Mineralogist 79, 340–352.
- 1293 Sjöqvist, A., Cornell, D., Andersen, T., Erambert, M., Ek, M., Leijd, M.,
1294 2013. Three compositional varieties of rare-earth element ore: Eudialyte-

- 1295 group minerals from the Norra Kärr alkaline complex, Southern Sweden.
1296 Minerals 3, 94–120. doi:10.3390/min3010094.
- 1297 Sørensen, H., 1992. Agpaitic nepheline syenites: a potential source of
1298 rare elements. Applied Geochemistry 7, 417–427. doi:10.1016/0883-
1299 2927(92)90003-L.
- 1300 Spera, F.J., Bohrson, W.A., 2001. Energy-constrained open-system mag-
1301 matic processes I: General model and energy-constrained assimilation and
1302 fractional crystallization (EC-AFC) formulation. Journal of Petrology 42,
1303 999–1018. doi:10.1093/petrology/42.5.999.
- 1304 Stevens, J., 1996. Applied multivariate analysis for the social sciences.
1305 Lawrence Erlbaum, Mahwah, NJ.
- 1306 Sun, C., Liang, Y., 2012. Distribution of REE between clinopyroxene and
1307 basaltic melt along a mantle adiabat: Effects of major element composi-
1308 tion, water, and temperature. Contributions to Mineralogy and Petrology
1309 163, 807–823. doi:10.1007/s00410-011-0700-x.
- 1310 Thirlwall, M.F., Singer, B.S., Marriner, G.F., 2000. ^{39}Ar - ^{40}Ar ages and
1311 geochemistry of the basaltic shield stage of Tenerife, Canary Islands,
1312 Spain. Journal of Volcanology and Geothermal Research 103, 247–297.
1313 doi:10.1016/S0377-0273(00)00227-4.
- 1314 Troll, V., Schmincke, H., 2002. Magma mixing and crustal recycling recorded
1315 in ternary feldspar from compositionally zoned peralkaline ignimbrite
1316 'A', Gran Canaria, Canary Islands. Journal of Petrology 43, 243–270.
1317 doi:10.1093/petrology/43.2.243.

- 1318 Van Orman, J.A., Grove, T.L., Shimizu, N., 2001. Rare earth element diffu-
1319 sion in diopside: influence of temperature, pressure, and ionic radius, and
1320 an elastic model for diffusion in silicates. Contributions to Mineralogy and
1321 Petrology 141, 687–703. doi:10.1007/s004100100269.
- 1322 Walker, D., Kirkpatrick, R.J., Longhi, J., Hays, J.F., 1976. Crystallization
1323 history of lunar picritic basalt sample 12002: Phase-equilibria and cooling-
1324 rate studies. Bulletin of the Geological Society of America 87, 646–656.
1325 doi:10.1130/0016-7606.
- 1326 Watson, E.B., 1979. Zircon saturation in felsic liquids: Experimental results
1327 and applications to trace element geochemistry. Contributions to Miner-
1328 alogy and Petrology 70, 407–419. doi:10.1007/BF00371047.
- 1329 Weidner, D.J., Vaughan, M.T., 1982. Elasticity of pyroxenes: Effects of
1330 composition versus crystal structure. Journal of Geophysical Research 87,
1331 9349–9353.
- 1332 Wiesmaier, S., Troll, V.R., Carracedo, J.C., Ellam, R.M., Bindeman, I.,
1333 Wolff, J.A., 2012. Bimodality of lavas in the Teide–Pico Viejo Succession
1334 in Tenerife—the role of crustal melting in the origin of recent phonolites.
1335 Journal of Petrology 53, 2465–2495. doi:10.1093/petrology/egs056.
- 1336 Wood, B.J., Blundy, J.D., 1997. A predictive model for rare earth
1337 element partitioning between clinopyroxene and anhydrous silicate
1338 melt. Contributions to Mineralogy and Petrology 129, 166–181.
1339 doi:10.1007/s004100050330.

- 1340 Wood, B.J., Blundy, J.D., 2001. The effect of cation charge on crystal–melt
1341 partitioning of trace elements. *Earth and Planetary Science Letters* 188,
1342 59–71. doi:10.1016/S0012-821X(01)00294-1.
- 1343 Wood, B.J., Blundy, J.D., 2003. Trace element partitioning under crustal
1344 and uppermost mantle conditions: The influences of ionic radius, cation
1345 charge, pressure, and temperature, in: Carlson, R.W. (Ed.), *The Mantle*
1346 and Core: Treatise on Geochemistry. Elsevier. volume 2. chapter 2.09, pp.
1347 395–424. doi:10.1016/B0-08-043751-6/02009-0.
- 1348 Wood, B.J., Blundy, J.D., 2014. Trace element partitioning: The influences
1349 of ionic radius, cation charge, pressure, and temperature, in: Carlson,
1350 R.W. (Ed.), *The Mantle and Core: Treatise on Geochemistry: Second Edi-*
1351 *tion*. Elsevier. chapter 3.11, pp. 421–445. doi:10.1016/B978-0-08-095975-
1352 7.00206-0.
- 1353 Wood, B.J., Trigila, R., 2001. Experimental determination of aluminous
1354 clinopyroxene–melt partition coefficients for potassic liquids, with applica-
1355 tion to the evolution of the Roman province potassic magmas. *Chemical*
1356 *Geology* 172, 213–223. doi:10.1016/S0009-2541(00)00259-X.
- 1357 Workman, R.K., Hart, S.R., 2005. Major and trace element composition of
1358 the depleted MORB mantle (DMM). *Earth and Planetary Science Letters*
1359 231, 53–72. doi:10.1016/j.epsl.2004.12.005.
- 1360 Wörner, G., Beusen, J.M., Duchateau, N., Gijbels, R., Schmincke, H.U.,
1361 1983. Trace element abundances and mineral/melt distribution coefficients

- 1362 in phonolites from the Laacher See volcano (Germany). Contributions to
1363 Mineralogy and Petrology 84, 152–173. doi:10.1007/BF00371282.
- 1364 Xu, C., Kynicky, J., Chakhmouradian, A.R., Campbell, I.H., Allen, C.M.,
1365 2010. Trace-element modeling of the magmatic evolution of rare-earth-rich
1366 carbonatite from the Miaoya deposit, Central China. Lithos 118, 145–155.
1367 doi:10.1016/j.lithos.2010.04.003.
- 1368 Yang, L., van Hinsberg, V.J., Samson, I., 2018. A new method to deconvolute
1369 binary mixture in LA-ICP-MS analyses to quantify the composition of
1370 phases smaller than the laser spot size. Journal of Analytical Atomic
1371 Spectrometry 33, 1518–1528. doi:10.1039/C8JA00078F.
- 1372 Yao, L., Sun, C., Liang, Y., 2012. A parameterized model for REE distri-
1373 bution between low-Ca pyroxene and basaltic melts with applications to
1374 REE partitioning in low-Ca pyroxene along a mantle adiabat and dur-
1375 ing pyroxenite-derived melt and peridotite interaction. Contributions to
1376 Mineralogy and Petrology 164, 261–280. doi:10.1007/s00410-012-0737-5.
- 1377 Zhang, Y., Ni, H., Chen, Y., 2010. Diffusion data in silicate melts. Reviews
1378 in Mineralogy and Geochemistry 72, 311–408. doi:10.2138/rmg.2010.72.8.

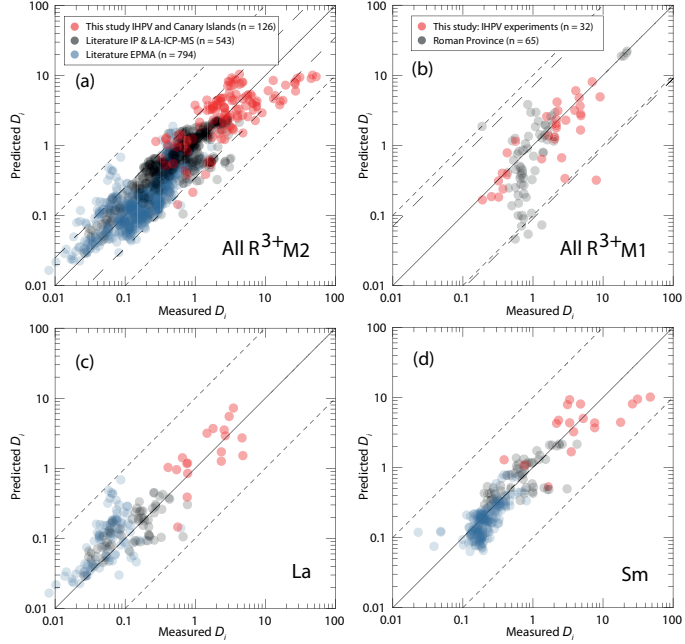


Figure 13: Measured clinopyroxene–silicate melt partition coefficients for 3+ cations vs. those predicted by our empirical model. (a) shows a comparison between measured partition coefficients and model-derived values for the M2 site of clinopyroxene. Hard dashed lines represent 95% confidence intervals of the model, and correspond to maximum uncertainties of factor ± 2.5 . Fine dashed lines represent 1 order of magnitude uncertainty (extreme outliers for M2 model). Partition coefficients in this diagram are the REE La to Er for our IHPV experiments, Canary Islands rocks, and literature data from the Roman Province (Wood and Trigila, 2001; Fedele et al., 2009; Mollo et al., 2013, 2016), and all the REE plus Y for the rest of the data compilation (Bédard, 2014), which is split by analytical methodology. (b) shows performance of the predictive model for the M1 site that is calibrated for alkaline magmatic systems, and includes data from our IHPV experiments and the Roman Province (Fedele et al., 2009; Mollo et al., 2013, 2016). Maximum uncertainties at the 95% confidence interval are a factor of ± 7 , higher than for the M2 site because of the smaller calibrating data set. (c) performance of the M2 site model for La, and (d) for Sm.

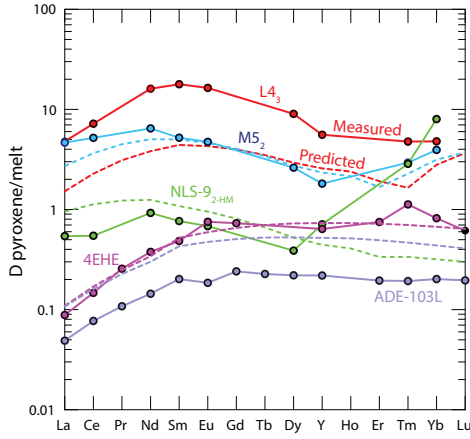


Figure 14: Measured and predicted element-partition coefficients for REE^{3+} . The model does not introduce notable radius-dependent biases, except for in our high-aegirine clinopyroxene (NLS-9₂-HM in green) for which D_{HREE} are strongly underpredicted, owing to inaccurate return of D_0^{M1} . Shown for comparison are two diopside–melt pairs: 4EHE from Hill et al. (2000), grown from a synthetic (NCMAS) basaltic andesite composition and ADE-103L from Lofgren et al. (2006) grown from a picritic composition based on the Angra dos Reis meteorite.

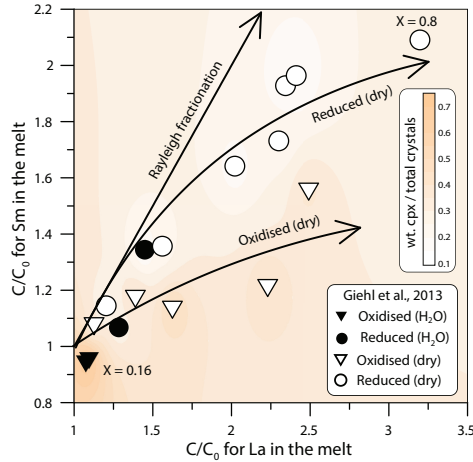


Figure 15: Model enrichment paths for La and Sm in residual melts during fractional crystallisation of a MiKa dyke composition (Gardar Province, Greenland, see Marks and Markl 2003). Phase relations and clinopyroxene compositions are from Giehl et al. (2013) and pertain to both oxidising and reducing conditions ($\log f\text{O}_2 = \Delta\text{QFM} - 3$ and +1), nominally dry to water bearing (to 3 wt.% H_2O at 1 kbar). Colour shading indicates the weight fraction of clinopyroxene within the crystallising assemblage. Bold arrows indicate residual enrichment pathways for the REE in the melt for Rayleigh fractionation (no incorporation into crystals), reduced, dry conditions, and oxidised dry conditions (the latter two are hand drawn fits to the data). For simplicity, this model does not consider REE incorporation into magnetite, alkali-feldspar, olivine, nepheline or aenigmatite, all phases generated in the experiments of Giehl et al. (2013) (see Larsen, 1979; Kovalenko et al., 1988; Mahood and Stimac, 1990).

¹³⁷⁹ **6. Tables**

Table 1: Major-element composition (in wt%) of starting materials for the internally heated pressure vessel experiments. The totals are calculated with all iron as FeO.

Dry starting glass compositions calculated from masses of reagents added [wt%]

Composition	SiO ₂	TiO ₂	Al ₂ O ₃	FeOT	MgO	CaO	Na ₂ O	K ₂ O	Total	(Na+K)/Al
L4	57.48	1.50	19.00	5.89	1.61	3.21	7.33	3.98	100.00	0.861
L5	61.24	0.68	19.51	3.77	0.43	0.91	8.63	4.84	100.00	0.996
M3	52.67	2.27	18.13	7.86	2.75	5.40	7.19	3.73	100.00	0.875
M4	56.35	1.47	18.63	5.77	1.58	3.15	8.48	4.57	100.00	1.014
M5	60.04	0.66	19.13	3.69	0.42	0.89	9.76	5.41	100.00	1.145
H4	54.80	1.43	18.12	5.62	1.54	3.06	10.07	5.38	100.00	1.236
H5	58.38	0.65	18.60	3.59	0.41	0.86	11.31	6.20	100.00	1.362

Water saturated glass compositions from superliquidus experiments (EPMA) [wt%]

L5	57.46	0.643	16.59	2.363	0.404	0.985	7.840	4.462	90.75	1.069
s.d. (n = 8)	0.299	0.087	0.210	0.059	0.035	0.050	0.175	0.132	0.351	0.017
rsd	0.52%	13.58%	1.26%	2.51%	8.70%	5.09%	2.23%	2.97%	0.39%	1.57%
H5	55.58	0.612	16.21	2.568	0.422	0.906	10.77	5.732	92.80	1.476
s.d. (n = 13)	0.327	0.057	0.221	0.113	0.044	0.049	0.205	0.154	0.417	0.028
rsd	0.59%	9.33%	1.36%	4.41%	10.44%	5.40%	1.90%	2.69%	0.45%	1.87%

Table 2: Summary of run conditions and run products for the internally-heated pressure vessel experiments.

Experiment	Setup	Pressure [bar]	Cooling ramp				(after ramp) [h,m]	Run products
			Rate °C /min	Cycle +10°C	TE-1/TE-3 [°C]	TE-2 (spl)s [°C]		
L4 ₃	IHPV RQ (f)	2038	1	Y	825	828	44h50m	Cpx + Ox + Ttn + Melt
L5 ₃	IHPV RQ (f)	2038	1	Y	825	828	44h50m	Cpx + Ox + Melt
M3 ₂	IHPV RQ	2020	1	Y	796/795	799	47h	Cpx + Ox + Bt + Melt
M4 ₄	IHPV RQ	2020	1	Y	796/795	799	47h	Cpx + Ox + Bt + Melt
M5	IHPV	2000	-	-	800	799	47h55m	Cpx + Bt + Fsp + Melt
M5 ₂	IHPV RQ	2000	-	-	700	689	45h45m	Cpx + Bt + Fsp + Melt
H4 ₂	IHPV	2000	-	-	800	799	47h55m	Cpx + Ttn + Melt
H5 ₂	IHPV RQ	2000	-	-	700	689	45h45m	Cpx + Bt + Fsp + Melt
H5 ₃	IHPV RQ	2020	-	-	651/649	648	46h15m	Cpx + Bt + Fsp + Melt
NLS-9	IHPV RQ	2020	1	Y	651/649	648	46h15m	Cpx + Ox + Melt
NLS-9 ₂ HM	IHPV RQ**	2000	1	Y	650	655	42h	Cpx + Ox + Fsp + Melt

(f) indicates failure of the rapid quench apparatus; ** indicates use of a haematite double capsule, for run conditions at the haematite-magnetite $f\text{O}_2$ buffer (Eugster and Wones, 1962). Cpx = clinopyroxene; Ox = spinel oxide; Ttn = titanite; Bt = biotite; Fsp = sanidine feldspar.

Table 3: Representative major-element compositions of clinopyroxene and melt for the performed internally heated pressure vessel experiments and Canary Islands phenocryst–glass pairs.

<i>Pyroxene</i>	L4 ₃	M3 ₂	M5 ₂	H5 ₃	NLS-9	NLS-9 ₂ HM	16-07 LMB	17-12 M. Samara	17-14 UMB-II	21-30 PV 2 ka
SiO ₂	44.70	40.73	47.31	46.95	50.73	51.90	52.43	51.77	51.81	52.50
TiO ₂	3.07	4.57	3.17	4.47	0.10	0.10	0.80	0.78	0.74	0.75
Al ₂ O ₃	5.23	9.26	3.08	3.10	2.46	2.96	1.33	1.24	1.27	1.22
FeO	13.31	11.72	18.84	16.95	28.14	28.61	9.71	9.62	10.51	10.02
MnO	0.01	0.01	0.01	0.00	0.25	0.17	0.78	0.84	0.91	0.81
MgO	9.09	9.28	5.55	6.05	0.05	0.07	12.30	12.64	12.07	11.88
CaO	19.49	22.17	16.11	15.29	5.88	3.14	21.90	21.76	21.52	22.02
Na ₂ O	2.27	1.01	4.34	4.97	9.86	11.45	1.18	1.17	1.38	1.19
K ₂ O	0.09	0.03	0.08	0.07	0.04	0.04	0.02	0.03	0.00	0.02
Total	97.25	98.78	98.49	97.85	97.49	98.45	100.44	99.85	100.22	100.42
<i>Glass</i>										
SiO ₂	58.79	57.29	57.45	54.91	58.17	58.14	60.38	55.10	59.08	60.04
TiO ₂	0.35	0.27	0.23	0.62	0.00	0.00	0.64	1.73	0.66	0.66
Al ₂ O ₃	17.35	19.14	16.69	16.06	18.55	19.41	19.96	18.30	19.68	19.79
Fe ₂ O ₃ (T)	2.35	1.35	1.01	3.16	1.67	1.91	3.65	7.22	4.02	3.96
FeO(T)	2.12	1.22	0.91	2.84	1.50	1.72	3.28	6.49	3.62	3.56
MnO	0.02	0.00	-	0.01	0.06	0.04	0.14	0.23	0.22	0.20
MgO	0.20	0.13	0.15	0.35	0.00	0.00	0.39	1.84	0.32	0.35
CaO	0.55	0.95	0.24	0.84	0.23	0.23	0.76	4.10	0.77	0.74
Na ₂ O	7.17	7.32	9.08	8.88	11.12	9.80	9.00	7.26	9.76	9.05
K ₂ O	4.68	4.10	4.68	5.30	1.51	2.51	5.41	4.09	5.45	5.57
Total	91.23	90.41	89.43	89.81	91.15	91.85	99.95	99.13	99.56	99.95
(Na+K)/Al	0.97	0.86	1.15	1.27	1.07	0.97	1.01	1.12	1.09	1.09

Table 4: Pyroxene-melt trace-element-partition coefficients for representative experiments and a natural phenocryst-glass pair.

-	L4 ₃		M3 ₂		M5 ₂		H5 ₃		NLS-9		NLS-9 ₂ HM		16-07-px4 LMB	
	D	σ	D	σ	D	σ	D	σ	D	σ	D	σ	D	σ
Li	0.250	0.016	0.126	0.009	0.419	0.034	0.427	0.024	0.274	0.029	0.251	0.025	0.157	0.021
Ga	0.364	0.022	0.567	0.020	0.190	0.022	-	-	-	-	-	-	0.216	0.020
Rb	0.005	0.002	0.018	0.003	0.010	0.006	0.013	0.002	0.026	0.015	-	-	0.000	0.000
Sr	0.828	0.045	0.282	0.024	1.433	0.111	0.997	0.091	0.321	0.045	0.269	0.111	0.732	0.293
Y	5.577	0.302	13.784	1.949	1.814	0.236	1.102	0.060	0.482	0.048	0.713	0.070	2.183	0.232
Zr	1.699	0.082	2.537	0.222	1.361	0.089	1.164	0.083	2.102	0.196	3.895	0.482	0.434	0.047
Nb	0.126	0.085	0.889	0.258	0.554	0.280	1.688	0.196	2.382	0.294	9.642	4.015	0.0062	0.0004
Cs	0.019	0.003	0.019	0.003	0.014	0.006	0.010	0.002	-	-	0.023	0.017	0.001	0.001
Ba	0.0364	0.0087	0.0373	0.0152	0.0388	0.0261	0.0288	0.0091	-	-	-	-	0.00004	0.00004
La	4.787	0.646	2.591	0.240	4.658	0.962	3.049	0.132	0.410	0.037	0.542	0.043	0.769	0.071
Ce	7.199	0.756	6.229	0.646	5.199	1.073	3.190	0.129	0.377	0.028	0.547	0.061	1.591	0.120
Nd	16.105	1.537	28.430	4.210	6.454	1.630	3.759	0.147	0.579	0.054	0.925	0.114	2.632	0.155
Sm	17.843	1.414	47.245	7.699	5.215	1.293	3.113	0.137	0.388	0.070	0.767	0.182	3.522	0.421
Eu	16.403	1.341	53.195	8.181	4.743	1.132	2.900	0.133	0.275	0.082	0.682	0.192	3.372	0.196
Dy	9.027	0.537	27.082	3.925	2.619	0.460	1.521	0.073	0.329	0.057	0.388	0.088	2.798	0.220
Tm	4.773	0.261	9.067	0.903	2.937	0.279	1.567	0.097	1.330	0.145	2.860	0.890	1.846	0.182
Yb	4.797	0.249	7.015	0.600	3.937	0.296	2.281	0.152	2.564	0.346	8.004	3.116	1.978	0.186
Hf	2.385	0.162	3.556	0.472	1.802	0.118	1.141	0.123	2.443	0.275	3.702	0.479	0.769	0.065
Ta	0.496	0.152	2.3694	0.6244	0.6502	0.2545	1.5654	0.2337	2.1082	0.1764	3.6854	0.6561	0.0153	0.0013
Pb	0.079	0.017	0.0587	0.0152	0.1142	0.0349	0.0199	0.0130	0.0884	0.0280	0.0564	0.0536	0.0203	0.0040
Th	0.201	0.034	0.3565	0.0419	0.3172	0.0321	0.2892	0.0239	0.0798	0.0240	0.0709	0.0276	0.0040	0.0003
U	-	-	0.0512	0.0331	0.1261	0.0272	0.0196	0.0103	0.0460	0.0245	0.0834	0.0342	0.0022	0.0003

Table 5: Coefficients for prediction of lattice-strain parameters for clinopyroxene M1 and M2 sites from clinopyroxene composition, temperature and pressure. Fitted vs. predicted lattice-strain parameters and partition coefficients are in Figures 12–13 and full multiple linear regression reports are available as supplementary data file S4.

Model for $\text{Ln}D_0$ M2 site (n = 82)			Model for $\text{Ln}D_0$, M1 site (n = 16)		
Parameter	Coefficient	σ	Parameter	Coefficient	σ
Intercept	4.52	0.91	Intercept	5	1
M1Ti	6.8	3	TAl	4	0.5
M1Al - M1Fe ³⁺	1.6	0.6	M1Fe ²⁺	2.6	0.9
M2Fe ²⁺	-3.8	1.3	M2Na	-8	1
T [K]	-0.0035	0.0007	M2Ca	-3	2
TAl + TFe ³⁺	2.6	0.8			
R^2		0.647			0.959

Model for E_s , M2 site (n = 79)			Model for E_s , M1 site (n = 18)		
Parameter	Coefficient	σ	Parameter	Coefficient	σ
Intercept	247	44	Intercept	-2322	298
M1Al	-424	144	T [K]	3.2	0.4
M1Mg	-285	102	P [GPa]	-408	145
M1Ti	-1145	378	M1Mg	-800	212
M2Mg	-306	115			
P [GPa]	37	12			
TAl + TFe ³⁺	313	102			
XMg	336	102			
R^2		0.348			0.936

Model for r_0 , M2 site (n = 82)			Model for r_0 , M1 site (n = 16)		
Parameter	Coefficient	σ	Parameter	Coefficient	σ
Intercept	1.01	0.02	Intercept	0.79	0.03
M1Ti	0.16	0.05	P [GPa]	-0.017	0.005
M1Al-M1Fe ³⁺	-0.03	0.01	M2Mg	-0.48	0.06
M2Ca	0.09	0.02	M1Fe ³⁺	0.14	0.03
M2Na	0.14	0.02	M2Ca	-0.05	0.02
T [K]	-4.46E-05	1.22E-05			
R^2		0.846			0.987

1380 7. Supplementary figures

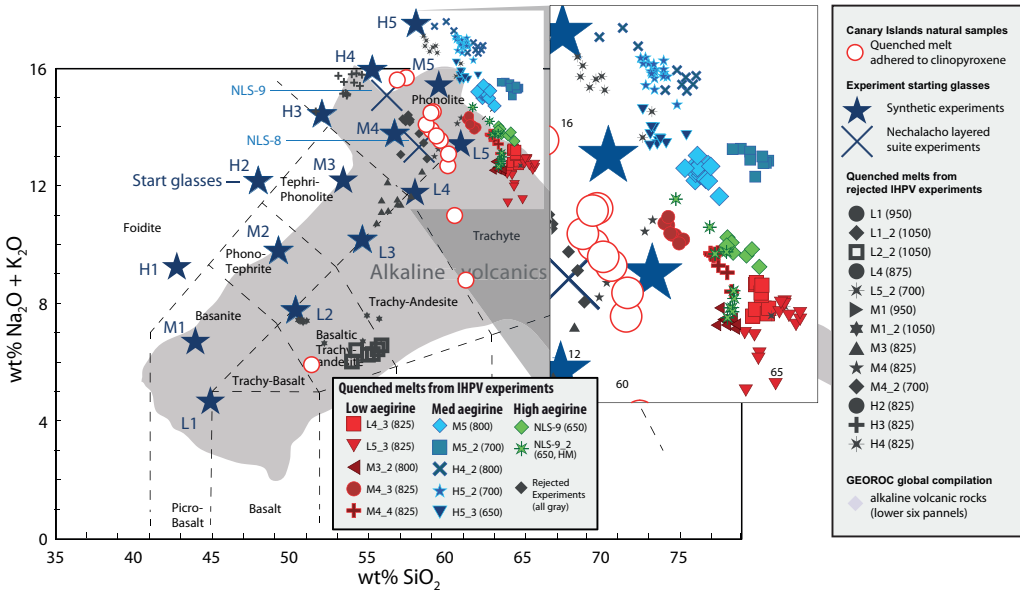


Figure S1: Total alkalies vs. silica diagram for glasses produced in internally heated pressure vessel experiments and adhered to Canary Islands clinopyroxene phenocrysts (Le Bas et al., 1986). Large stars indicate synthetic starting glass compositions as used in internally heated pressure vessel experiments (Table 1), whereas large crosses indicate the composition of powdered natural samples from the Nechalacho layered suite, NT, Canada that were used as starting materials for some experiments. The gray field indicates the compositional range expressed by alkaline volcanic provinces from around the world, sourced from the GEOROC database. Rejected experiments in dark gray are not discussed in the main text, and either did not produce clinopyroxene, produced crystals that were too small for analysis by LA-ICP-MS, or grew crystals during quench, hence preserving disequilibrium partitioning behaviour. Further diagrams showing major-element compositions for the quenched melts and the starting glasses are in Fig S2.

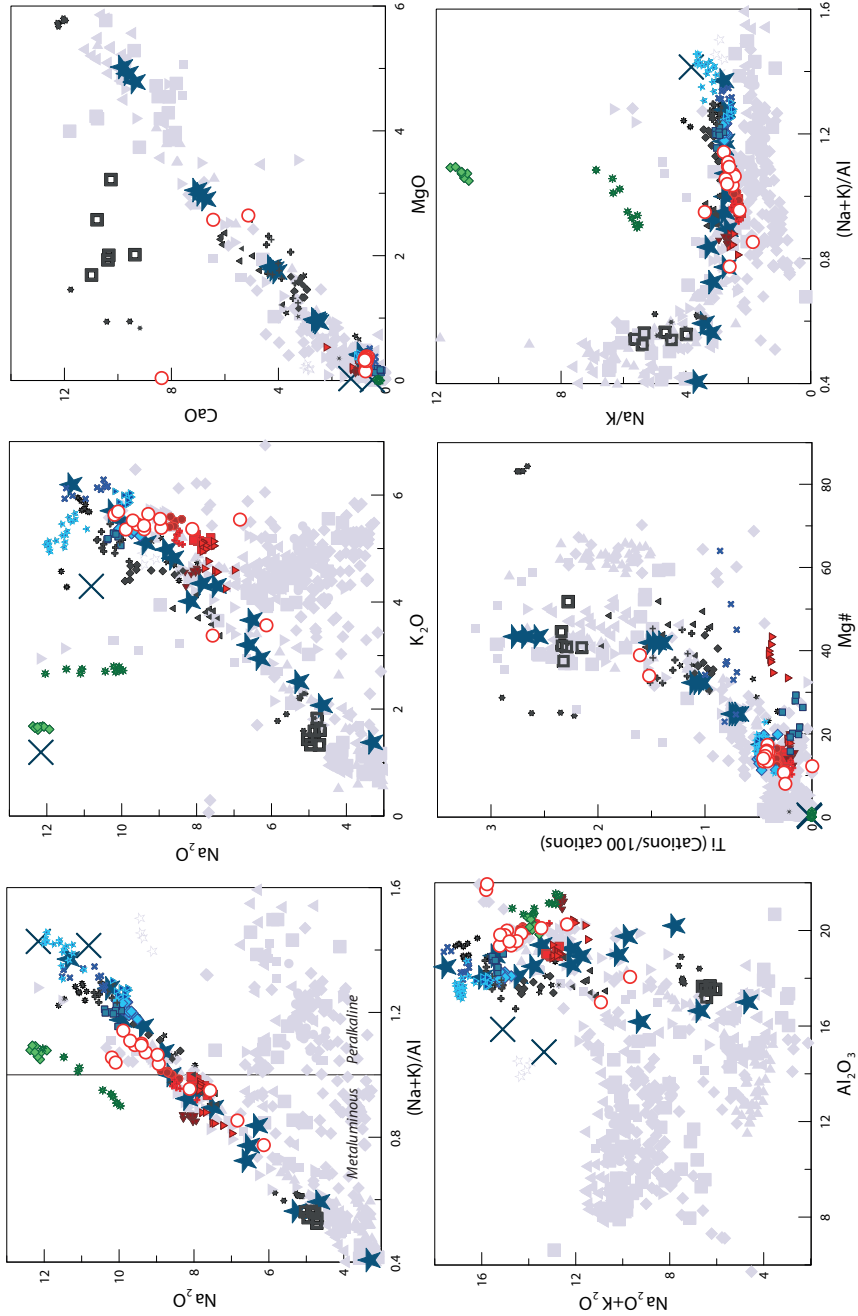


Figure S2: Major-element compositions for glass produced in the internally heated pressure vessel experiments and adhered to clinopyroxene phenocrysts from the Canary Islands. Symbols as in Fig. S1.

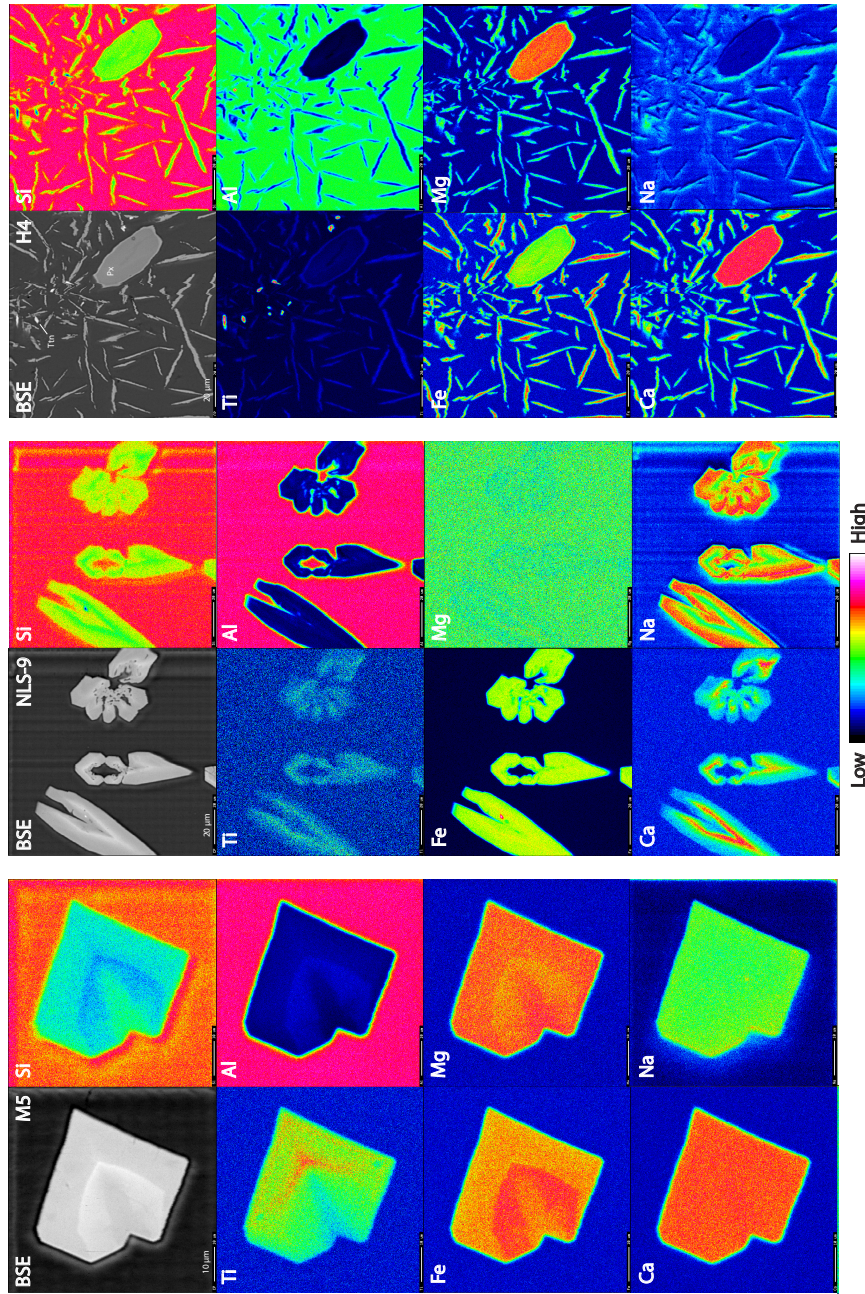


Figure S3: Element maps of clinopyroxene from internally heated pressure vessel experiments. M5 clinopyroxene have a sharp internal boundary that reflects feldspar saturation and are subtly zoned. NLS-9 clinopyroxene are more strongly zoned with swallowtail and hopper textures and rare inclusions of magnetite (cf. Walker et al., 1976; Lofgren, 1989; Shea and Hammer, 2013). H4 clinopyroxene (P_X) display a bimodal crystal size distribution and occur with titanite (Tn). The bimodal crystal size distribution is due to a temperature perturbation during run, and renders this experiment unsuitable for this element-partitioning study.

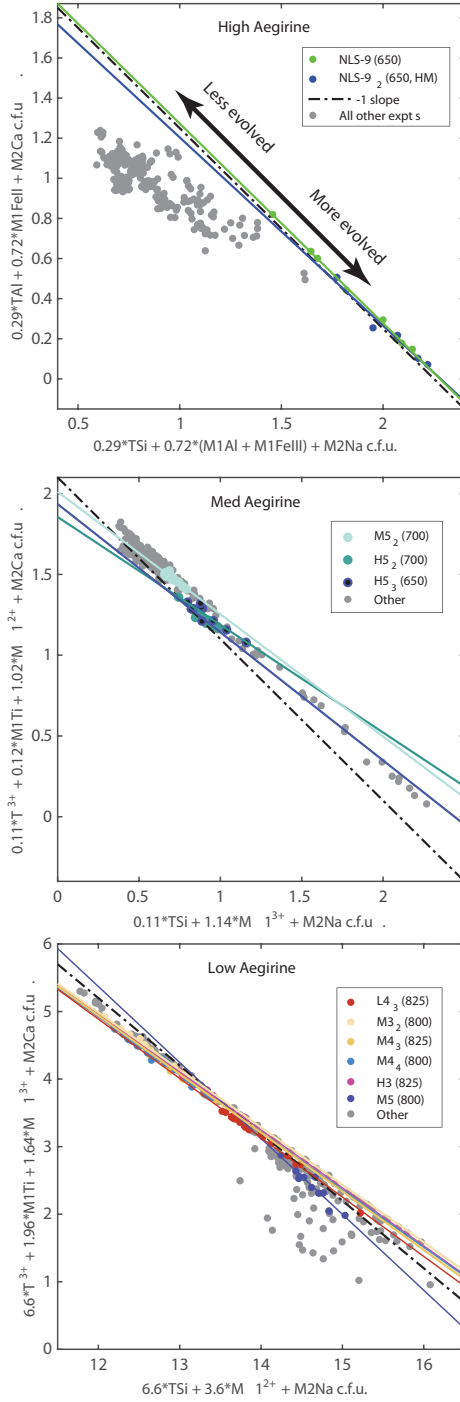


Figure S4: Major-element exchange mechanisms for (a) high, (b) medium and (c) low-aegirine clinopyroxene generated in internally heated pressure vessel experiments. Each individual plotted point represents an electron-microprobe analysis. Iron in the clinopyroxene was assigned to 2+ or 3+ valence following Droop (1987), then major-element cations were assigned to sites following Morimoto (1989, see supplement S5). Axes were defined by linear regressions between site-assigned major-element abundances, which have been checked for consistency in total site-occupancy and for charge.

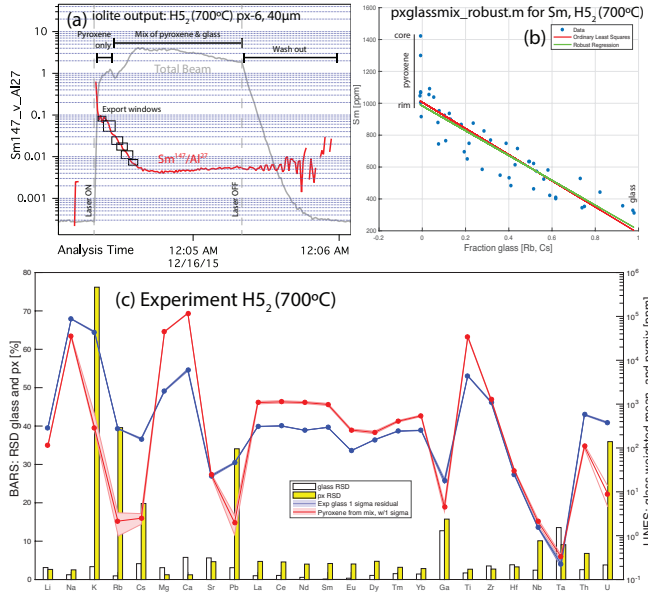


Figure S5: An example of the robust regression data reduction scheme for laser-ablation ICP-MS analyses of glass and clinopyroxene mixtures. (a) Time series of laser-ablation data, showing traces for Sm/Al (red) and total beam intensity (gray). The laser beam often ablated through the small clinopyroxene crystals, returning a mixed signal that was exported from the iolite data reduction software in short time windows as shown. Data were then normalised to the sum of major-element concentrations and mixes were deconvolved using a robust regression script written in MATLAB. (b) An example output diagram for the robust regression data reduction scheme. Clinopyroxene–glass mixing ratios were constrained by strongly incompatible elements Rb and Cs. For each element, a robust linear regression was defined between the fraction of glass in the mixture and element concentration. The intercept of this regression with zero glass returned the trace-element concentrations in the clinopyroxene. Uncertainty with this technique is typically below 10 % relative (median 9.3 % at the 1σ level). In this example, the Sm-rich core of a zoned clinopyroxene crystal is effectively rejected during data processing, and the derived Sm concentration for the clinopyroxene is therefore closer to that of the clinopyroxene rims that are in equilibrium with the adjacent quenched melt. (c) A quality control diagram output from the MATLAB data reduction scheme showing the concentrations of various elements in the glass and clinopyroxene (lines) and the uncertainty on these concentrations expressed as a relative standard deviation (δ_{bars}). Derived partition coefficients (D_i) are the mass concentration of element ' i ' in clinopyroxene divided by that in the adjacent quenched melt. Residuals for the D_i values were calculated using uncertainties derived from the clinopyroxene and glass analyses to calculate minimum and maximum partition coefficients at the 1σ level. These are reported in Table 4 and Supplement S1.

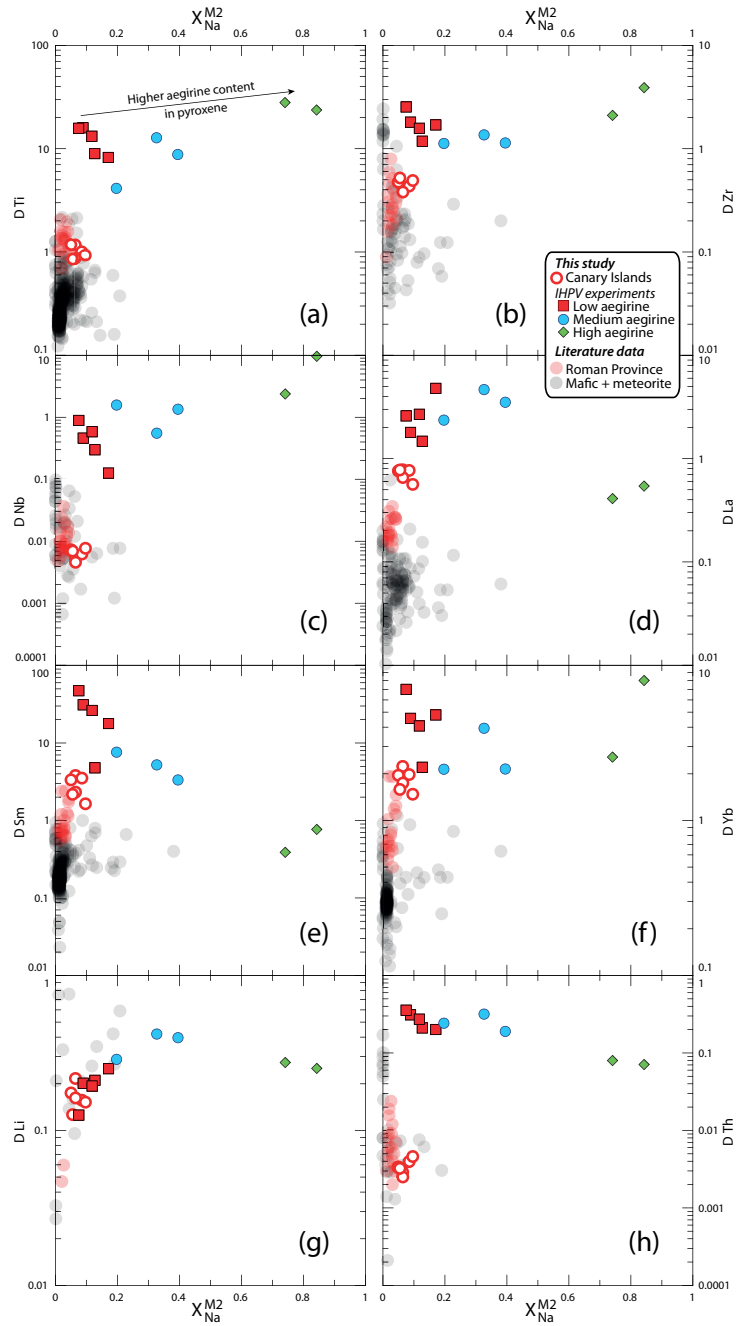


Figure S6: Element partitioning coefficients for HFSE (Ti, Zr, Nb), REE (La, Sm, Yb) and TE (Li, Th) vs. X_{Na}^{M2} . Literature values ($n = 411$), including those from the Roman Province, Italy, are from the compilation of Bédard (2014).

₁₃₈₁ **8. Electronic appendices**

xlsx

Table S1: Electronic appendix (.xlsx file) containing experiment starting glass compositions, experiment run conditions, mineral abundances in experimental charges, compositions of reference materials used for EPMA and LA-ICP analyses, major-element concentrations for experiment glasses and clinopyroxene, partition coefficients and fitted lattice-strain parameters.

kml

Table S2: Electronic appendix (.kml file) containing field locations for the Canary Islands samples.

kml

Table S3: Electronic appendix (.xlsx file) containing electron-microprobe transects across experiment clinopyroxene for Ce, Mg and Fe. The data indicate that $D_{Ce}^{px/melt}$ values determined from our experiments are overestimates, but only by up to 25%. Sector zoning in the clinopyroxene appears to have a larger impact on apparent Ce partitioning behaviour than growth zoning.

pdf

Table S4: Electronic appendix (.pdf file) containing multiple linear regression reports from the stepwise fitting of 3+ cation lattice-strain parameters for the predictive model for element-partitioning (39 pages).

xlsx

Table S5: Electronic appendix (.xlsx file) containing a numerical model for prediction of clinopyroxene/melt element-partitioning coefficients for ions of 3+ valence. Required input data are major-element oxide compositions for clinopyroxene, pressure and temperature. The model for the M2 site is calibrated for application to systems of basaltic to peralkaline phonolite composition. The model for the M1 site is calibrated for use on alkaline to weakly peralkaline systems where the aegirine mol% in clinopyroxene does not exceed 50.

1382 **9. Supplement: Chemical heterogeneity and the approach to equi-**
1383 **librium during the experiments**

1384 *9.1. Attainment of equilibrium in the Canary Islands rocks*

1385 The Canary Islands trace-element partition-coefficients presented here
1386 were determined from euhedral, blade-shaped crystals free of melt inclu-
1387 sions and chemical zonation. The corresponding quenched melt was in direct
1388 contact with these crystals and shows no zonation in backscattered electron
1389 images (Fig. 1). While equilibrium conditions are challenging to confirm for
1390 a natural volcanic system, the euhedral forms, chemical homogeneity of crys-
1391 tals, and congruency between samples from separate eruptions suggest that
1392 the crystals grew in a stable environment, and were not subject to chemical
1393 or physical perturbations during growth (Fig. 6).

1394 *9.2. Attainment of equilibrium in the experiments*

1395 Experiments used to determine trace-element partition-coefficients must
1396 have attained, or at least closely approached, chemical equilibrium. Un-
1397 fortunately no experiments are able to determine equilibrium trace-element
1398 partition-coefficients *sensu stricto* because reversal experiments, where a
1399 clinopyroxene re-equilibrates with a melt, are not possible owing to slug-
1400 gish diffusion of most elements through the clinopyroxene structure (Van
1401 Orman et al., 2001; Zhang et al., 2010). The following two sections discuss
1402 some analytical and experimental biases that must be considered when deter-
1403 mining mineral-melt trace-element partition-coefficients from crystallisation
1404 experiments.

1405 *9.2.1. The formation of diffusive boundary layers*

1406 A potential barrier to chemical equilibration during crystallisation is the
1407 formation of a diffusive boundary layer within the melt adjacent to growing
1408 crystals. In a perfect equilibrium case there are no compositional gradients
1409 in the melt at any time during crystal growth. However in reality the growth
1410 of crystals depletes compatible elements from the melt and residually en-
1411 riches incompatible elements. Theoretically, this process of crystal growth
1412 results in formation of a (potentially ephemeral) diffusive boundary layer in
1413 the melt directly adjacent to the crystal that is depleted with respect to
1414 compatible elements and enriched with respect to those that are incompat-
1415 ible (Lu et al., 1995). The composition of such a diffusive boundary layer
1416 depends on both the relative enrichment or depletion of elements during the
1417 crystallisation process, and the rate at which these elements diffuse through
1418 the melt. Rapidly-diffusing elements with partition-coefficients close to unity
1419 will have concentrations closest to that of the bulk melt.

1420 Experiments designed to investigate trace-element-partitioning behaviour
1421 might employ slow cooling rates to limit the development of diffusive bound-
1422 ary layers, thus forming crystals from melt that is closer in composition to
1423 that of the bulk experiment. Such experiments then run into another prob-
1424 lem, in that significant crystallisation may occur at temperatures above that
1425 of the final run temperature. Rapidly-cooled experiments circumnavigate
1426 this issue, but may form relatively more pronounced diffusive boundary layers
1427 during crystal growth that become ‘flattened out’ during the homogenisation
1428 stage of the experiment.

1429 Numerous diffusion data have been gathered for silicate melts over the

1430 past few decades, and a comprehensive review is given by Zhang et al.
1431 (2010). Diffusion of trace-elements through water-saturated peralkaline melts
1432 is rapid, owing to their depolymerised structure. For example Lanthanum
1433 diffusion-coefficients are 6 orders of magnitude higher than for water-saturated
1434 granitic compositions of a similar temperature (compare Rapp and Watson,
1435 1986; Behrens and Hahn, 2009). This rapid diffusion serves to minimise the
1436 formation of diffusive boundary layers adjacent to growing crystals in our
1437 experiments. Coupled diffusion mechanisms complicate the application of
1438 measured single-element diffusion-coefficients to a crystallising system (Grove
1439 et al., 1984; Liang et al., 1994; Costa et al., 2003). Here, the diffusive flux of
1440 trace-elements may be coupled to gradients in major-element concentration
1441 within the melt.

1442 To investigate the impact of diffusive effects on trace-element-partitioning
1443 between clinopyroxene and melt, Mollo et al. (2013) performed crystallisa-
1444 tion experiments on trachybasaltic melts at a range of cooling rates (2.5–
1445 50°C / hr). Rapid cooling rates result in depletions of Si, Ca and Mg in
1446 the clinopyroxene that are compensated for by enrichments in Al, Na and
1447 Ti. Regardless of cooling rate, Ounma parabolae could be fitted through
1448 isovalent sets of partition-coefficients, indicating that crystal-lattice-effects
1449 dominated over those associated with the formation of diffusive boundary
1450 layers and that local equilibrium was achieved at the time of crystallisa-
1451 tion. In their rapidly-cooled experiments Mollo et al. (2013) found apparent
1452 clinopyroxene/melt trace-element partition-coefficients that varied with iden-
1453 tical crystal-chemical systematics to true equilibrium partition coefficients,
1454 the magnitude of both sets of trace-element partition-coefficients following

1455 the ^{IV}Al content of the clinopyroxene (ibid., their Fig. 9). Deviations of
1456 the partition coefficient of several orders of magnitude can be obtained only
1457 when rapidly growing crystals entrap small portions of the diffusive boundary
1458 layer that are found as minute melt inclusions randomly distributed in the
1459 mineral phase (Kennedy et al., 1993). In this extreme case, partitioning be-
1460 haviour is obviously influenced by contamination phenomena and no Onuma
1461 parabolae can be derived. As Onuma parabolae could successfully be fitted
1462 through partitioning data for all of our presented experiments (see following
1463 sections), and no melt inclusions were observed in optical and electron imag-
1464 ing, we infer that our data were not affected by the presence of such melt
1465 inclusions, and that they may be compared directly with partitioning data
1466 derived from experiments that employed slower cooling rates.

1467 *9.2.2. Chemical zonation in the experiment clinopyroxene: Theoretical frame-
1468 work*

1469 Trace-elements diffuse slowly through the clinopyroxene structure relative
1470 to that of the melt (Van Orman et al., 2001; Zhang et al., 2010), therefore no
1471 re-equilibration of trace-elements takes place on an experimental time scale.
1472 Strictly speaking, clinopyroxene only record true equilibrium conditions at
1473 their outermost rim. Experiments designed for the derivation of equilibrium
1474 partition coefficients ideally minimise bias by limiting the fraction of crystalli-
1475 sation, producing minerals that are as homogeneous as possible. Currently
1476 available *in situ* analytical techniques for trace-element abundances, such as
1477 LA-ICP-MS and SIMS, are limited in terms of minimum beam-size to ~ 10
1478 μm ; chemical zonation, however subtle, will be continuous from the core to
1479 the rim of the mineral. Consequently, no experimentally-derived partition-

1480 coefficients record chemical equilibrium *sensu stricto*, but properly conducted
1481 experiments may closely approximate this state.

1482 Because only the very rim of a crystal records chemical equilibrium with
1483 the adjacent melt, and some internal portions of the minerals must be sam-
1484 pled during *in-situ* analyses all experimentally-determined trace-element partition-
1485 coefficients are biased toward higher values for compatible elements and lower
1486 values for incompatible elements. The magnitude of these biases depends
1487 on the fraction of crystallisation in the experiment, the true equilibrium
1488 partition-coefficient of that element, as well as the proportion of each growth-
1489 zone sampled during the *in-situ* analysis. Fortunately *in-situ* chemical anal-
1490 yses preferentially sample the mantle and rim of zoned crystals because few
1491 analyses section a crystal perfectly through the core. As a result there is a
1492 sampling bias toward equilibrium mineral compositions.

1493 Consider a hypothetical experimental system in which 20% of the melt
1494 crystallises as a single mineral, and where the chemical analyses of that
1495 mineral are truly bulk averages of that mineral composition. An incompatible
1496 element with a true equilibrium partition coefficient of 0.1 would return a
1497 measured partition coefficient of 0.09, a small bias because the concentration
1498 of that incompatible element in the melt changed only subtly during the
1499 course of crystallisation. For compatible elements with true D_i values of
1500 ~ 10 , measured partition coefficients can be a factor of 2–3 higher than true
1501 partition coefficients, because their concentration in the melt changes more
1502 than an incompatible element during the course of crystallisation.

1503 Further complexity is introduced in systems that crystallise multiple min-
1504 erals simultaneously. In the case of experiment M3₂, the REE are compatible

1505 in clinopyroxene, but are incompatible in biotite and oxides (e.g. Mahood and
1506 Stimac, 1990; Schmidt et al., 1999). The REE have therefore been residually
1507 enriched in the melt phase by the crystallisation of biotite and oxide miner-
1508 als, while simultaneously being depleted from the melt by crystallisation of
1509 clinopyroxene. These two competing processes serve to minimise the effect of
1510 fractional crystallisation on the concentration of trace-elements in the melt
1511 and consequently derived REE partition-coefficients between clinopyroxene
1512 and melt will be closer to true equilibrium values.

1513 *9.2.3. Implications of the cerium zonation across the experiment clinopyrox-
1514 ene*

1515 Electron-microprobe analyses offer a smaller minimum beam-size than
1516 LA-ICP-MS systems at the expense of precision and of number of elements
1517 that may be analysed simultaneously. This higher spatial resolution permit-
1518 ted investigation of the zonation of Ce concentrations within the experiment
1519 clinopyroxene, with Ce as a proxy for the other compatible elements.

1520 The magnitude of concentric growth zoning in the experiment clinopyrox-
1521 ene was examined by averaging bulk and rim compositions across multiple
1522 sector-zoned grains within each experiment. The median Ce counts divided
1523 by the rim Ce counts was 1.04 for experiment M3₂, 1.08 for experiment M5
1524 and 1.12 for the fluorine-bearing experiment M3-1.25F (see ?). Contrary to
1525 theory discussed above, the subtly (3%) crystallised experiment M5 shows a
1526 greater variation in core-to-rim Ce content than the more heavily (?? TO
1527 ADD%) crystallised experiment M3₂. Furthermore, the $D_{Ce}^{cpx/melt}$ for experi-
1528 ment M3₂ (6.2) is approximately double that for experiment M5 (see discus-
1529 sion below), which should further promote the formation of Cerium zonation

1530 in the clinopyroxene during crystallisation. Consequently it is possible that
1531 many existing experimentally-derived trace-element partition-coefficients are
1532 systematically offset from true equilibrium values.

1533 If Cerium is used as a proxy for the behaviour of compatible elements
1534 in our experimental system, then apparent partition coefficients derived for
1535 these elements via LA-ICP-MS are systematically offset to higher values by 4–
1536 8%. Such a systematic bias is small, relative to the variation in clinopyroxene–
1537 melt partition coefficients within our sample set, as well as in the literature.
1538 The effect of crystal zonation on incompatible element concentrations was
1539 not measured, but as outlined in the theoretical framework above, this effect
1540 should be smaller than that for the compatible elements. No correction factor
1541 has been applied to the data presented in the figures below, or in Tables 4
1542 and S1.